#### Title

Pre-curved, fiber-reinforced actuators enable pneumatically efficient replication of complex biological motions.

#### **Authors**

Lucy Hu<sup>1,2</sup>, Dominik Gau<sup>3</sup>, James Nixon<sup>4</sup>, Melissa Klein<sup>5</sup>, Yiling Fan<sup>5</sup>, Gary Menary<sup>4</sup>, Ellen T. Roche<sup>1,2,5\*</sup>

#### **Affiliations**

- <sup>1</sup>Harvard-MIT Program in Health Sciences and Technology, Massachusetts Institute of Technology, Cambridge, MA, USA.
- <sup>2</sup>Institute of Medical Engineering and Sciences, Massachusetts Institute of Technology, Cambridge, MA, USA.
- <sup>3</sup> Department of Mechanical Engineering, Technical University of Munich, Garching, Munich, Germany
- <sup>4</sup>School of Mechanical and Aerospace Engineering, Queens University, Belfast, Northern Ireland, UK.
- <sup>5</sup>Department of Mechanical Engineering, Massachusetts Institute of Technology, Cambridge, MA, USA.
- \*Corresponding author. Email: etr@mit.edu

#### Abstract

Much of the research on bioinspired soft robotics has focused on capturing the interplay of biological form and function. However, existing soft robotic actuators are mostly made with linear or planar fabrication orientations that do not represent the resting geometry of complex biological systems, such as curved musculature. This work introduces the ability to create fiberreinforced actuators with pre-curved configurations. By tuning variables such as dimensions and fiber angles, an optimization algorithm can prescribe the mechanical fabrication parameters to create a fiber-reinforced actuator that can generate controlled motion to follow a desired input trajectory. Pre-curved configurations introduce an additional optimization parameter, the initial bend angle, allowing for a more accurate and robust algorithm and generating a median percenterror of less than 1%. With a customized software tool, we can take existing motion data from biological systems—such as medical imaging—and build soft robotic actuators optimized to replicate these trajectories. We can predict the motion of pre-curved actuators both analytically and numerically and replicate the motion experimentally, with excellent trajectory matching between the three. In constructing actuators that better match the native forms found within biological systems, we find that pre-curved actuators are more efficient than their initially straight counterparts. This pneumatic efficiency allows for the use of control systems with lower power and precision, lowering the economic cost of the associated control hardware, while more accurately replicating the biological motion. Taking two examples from biology, that of the human diaphragm during respiration and that of a jellyfish bell during locomotion, we design and generate fiber reinforced actuators to mimic these motions.

#### **Objective**

Soft robotics are often looked to as a technology to create actuators to replicate bioinspired motion. <sup>1–4</sup> However, the inherently complex nature of soft materials makes creating tunable and controllable motion a key challenge. In order to address this issue, many have worked towards modeling and solving the forward kinematics problem. <sup>5–8</sup> In order to utilize the results of this body of work, a design tool software has previously been developed to combine analytical modeling and computational optimization in order to find optimal design parameters to follow a given jointed-segment trajectory, using the motion of a finger as the baseline inspiration. <sup>9</sup> Although this tool is robustly developed for the purposes of following the motion of a finger, advances are required to expand utility to take into consideration geometric complexity. The objectives of this work are to update the analytical model, cross-validate the model with FEA and experimental results, and modify the algorithm to allow for pre-curved fiber-reinforced actuators to reduce optimization error and increase the pneumatic efficiency for the replication of biological motions.

The natural world is filled with examples of curved and geometrically complex actuators. Due to the interdependence of form and function, this geometric complexity is key to bioinspired systems. Specific examples within the human body include the curved muscles that wrap around and stabilize the spine <sup>10</sup> and the domed muscle of the diaphragm. <sup>11</sup> The animal kingdom also provides key examples, such as the dome shape of a jellyfish's bell. <sup>12</sup> In such examples, their resting geometries are key to their function.

The prior existing work assumes an initially straight fabrication geometry, which provides for ease of manufacturing. However, this boundary condition sacrifices the capacity to capture the functional geometric complexity of curved and domed structures. A side effect of this imposed linear resting state is that the actuators do not utilize a portion of the pneumatic range, increasing the technical requirements of the pneumatic system that controls actuation. This pneumatic inefficiency subsequently drives up the costs of corresponding control systems. The term "pneumatic efficiency" refers to the ratio of useful work—which in this case is dynamic motion replication—to the pneumatic demands required of the system. Our work removes the unnecessary boundary condition of an initially straight geometry and adds an additional optimization parameter, enabling the creation of fiber-reinforced actuators with an initially curved configuration, which we refer to as pre-curved actuators. By investing in a slightly more complex fabrication process, this update to actuators reaps cost-saving returns in creating pneumatically-efficient actuators that better capture the geometric complexities of biological motions.

#### Introduction

Fiber-reinforced actuators belong to a class of soft robotic actuators called fluidic elastomer actuators. The actuators consist of a soft elastomeric body with an embedded fluid cavity; they are actuated via pressurization of the fluidic cavity. To create tunable deformation of this elastomeric body, inextensible fibers are wrapped around cylindrical actuators to generate controlled anisotropy. The previous work characterized the tunability of cylindrical fiber-reinforced actuators and categorized them into their principal motions: extending, twisting, and bending. Extending actuators lengthen or contract, depending on the fiber angle. Twisting

actuators generate a rotation about the axis along the center of the actuator. Bending actuators exist as two-material elastomer segments in which one elastomer is stiffer than the other. The less stiff material preferentially deforms causing a bending moment to generate a bend angle,  $\psi$ . Here, we enhance these actuators by introducing another variable,  $\psi^{(0)}$ , the resting bend angle defined in reference to the starting bend angle inscribed by the initially concave side of the actuator. The introduction of  $\psi^{(0)}$  requires an update to the definition of bending segment types. Depending on the orientation of the stiffer and less stiff elastomers, we subcategorize bending segments into flexing and counter-flexing actuators based on their pressure response  $\left(\frac{d\psi}{dP}\right)$ , seen in Fig. 1A, which is distinct from their time response. Flexing actuators are defined by their positive bend angle pressure response  $(\frac{d\psi}{dP} > 0)$  for positive pressures resulting in an initially "closing" motion  $(\frac{d\psi}{dt} > 0)$ . Contrastingly, counter-flexing actuators are defined by their negative bend-angle-pressure response  $(\frac{d\psi}{dP} < 0)$ , as they undergo an initially "opening" motion for positive pressures  $(\frac{d\Psi}{dt} < 0)$ . Note that counter-flexing actuators initially begin in an "opening" motion, however when the bend angle passes  $\psi = 0$  into the negative bend angles, the actuator will engage in what appears to be a "closing" motion as the bend angle magnitude increases although it is deforming in the negative direction. These actuator segments cannot be simply categorized as closing or opening due to this edge case.

The introduction of pre-curved actuator segments also complicates the geometrical considerations of the specified fiber angles. In the cylindrical actuator segments, the fibers take the three-dimensional form of a straight coil with a constant coil pitch. In order to define the fiber trajectory in pre-curved segments, we rely on referencing the circumferential angle,  $\varphi$ , which is the radial angle within the cross-sectional plane orthogonal to the longitudinal axis of the actuator. The seams that join the two different elastomers for bending actuator segments exist at  $\varphi = 90^{\circ}$  and  $\varphi = 270^{\circ}$ . The deformation of these elastomeric actuators is governed by the axial stress  $\sigma_{zz}$  in the material, see Fig. 1B. A given fiber of fiber angle  $\alpha$  for a pre-curved segment is defined by a point-wise creation of a helical trajectory with respect to the circumferential coordinate,  $\varphi$ , and the subsequent rotation around the center of curvature where for every infinitesimal circumferential cross-section, the local tangential fiber angle is asserted to be  $\alpha$  (see Fig. 1C). With the introduction of the initial curvature, the pitch varies along the circumferential angle, with the smallest pitch distance at  $\varphi = 0^{\circ}$ , the innermost material line on the initially concave side, and the largest pitch distance at  $\varphi = 180^{\circ}$ , the outermost material line on the initially convex side.

With the addition of pre-curved actuator segments, the computational optimization workflow is modified to include the new pre-curved segment types—flexion and counter-flexion—in addition to the new variable  $\psi^{(0)}$ , as seen in the workflow schematic in Fig. 1D. The computational optimization takes the desired bioinspired trajectory as an input, and couples the updated analytical model with a nonlinear least-squares optimization algorithm in MATLAB (Isqnonlin) to minimize the objective function which is the sum of errors for all configurations  $n_{config}$  and all associated actuator segment types  $n_{type}$  where type = [twist, link, flex, counterflex] between the desired parameters (twist  $(\theta)$ , link length (l) and bend angle  $(\psi)$ ) and the resultant parameters for a given pressure:

$$f(\underline{x}) = w_{twist} \sum_{j=1}^{n_{config}} \sum_{i=1}^{n_{twist}} \left| \theta_{i}^{(j)}(\underline{x}) - \hat{\theta}_{i}^{(j)} \right|^{2} + w_{link} \sum_{j=1}^{n_{config}} \sum_{i=1}^{n_{link}} \left| l_{link,i}^{(j)}(\underline{x}) - \hat{l}_{link,i}^{(j)} \right|^{2} + w_{flex} \sum_{j=1}^{n_{config}} \sum_{i=1}^{n_{flex}} \left| \psi_{flex,i}^{(j)}(\underline{x}) - \hat{\psi}_{flex,i}^{(j)} \right|^{2} + w_{counterflex} \sum_{j=1}^{n_{config}} \sum_{i=1}^{n_{config}} \left| \psi_{counterflex,i}^{(j)}(\underline{x}) - \hat{\psi}_{counterflex,i}^{(j)} \right|^{2}$$

$$+ w_{counterflex} \sum_{j=1}^{n_{config}} \sum_{i=1}^{n_{config}} \left| \psi_{counterflex,i}^{(j)}(\underline{x}) - \hat{\psi}_{counterflex,i}^{(j)} \right|^{2}$$

$$(1)$$

The optimization will output the multi-segment actuator design parameters, in vector  $\underline{x}$ , necessary for the fabrication and the actuation pressures to replicate the desired motion trajectory. The optimization algorithm relies on an input-dependent deviate-based weighting function. Further details about the optimization algorithm and weighting scheme can be found in the Supplementary Materials and Fig. S1. Given these parameters, we can follow a fabrication process, shown in Fig. 1E, to cast a silicone actuator with these given specifications.

# Materials and Methods Study Design

The overall objective of this work was to update the design optimization of fiber-reinforced actuators to allow for pre-curved actuators. Cross-validation between the analytical model, FEA, and two experimental methods provided the confidence to proceed with the analytical model. To generalize the effects of including non-zero  $\psi^{(0)}$  into the optimization, we simulated large data sets of randomized trajectories (n=28 for each case: opening and closing trajectories) and ran them through the optimization. Initially straight actuators were given the constraint of  $\psi^{(0)} = 0^{\circ}$ , while pre-curved actuators were given the constraint  $\psi^{(0)} \in (0^{\circ}, 180^{\circ}]$ . We measure the accuracy of the optimization via percent error between the desired input trajectory and the optimized output trajectory, and pneumatic efficiency via pressure range utilization and pneumatic surplus. Due to the long and manually intensive fabrication time, we opt to only fabricate the actuators of select cases. We use the optimization to replicate two cases of biological motion, the diaphragm and the jellyfish, as applications of this platform.

#### **Optimization algorithm**

The design optimization algorithm consists of an objective function which is minimized using a trust-region method which is carried out with the MATLAB function Isqnonlin (MathWorks, Natick, MA, USA). For the objective function to be optimized, the analytical equations for extending, twisting, flexing and counter-flexing actuators have to be solved for a given input trajectory, which is discretized in its link lengths  $l_{link}$ , bend angles  $\psi$  and twist angles  $\theta$  for a finite number of configurations. For every extending and twisting segment, the inflation-extension-torsion problem <sup>13,14</sup> is solved for the axial stretch and the angle of twist, respectively and is solved for the bend angle for every flexing and counter-flexing segment. The axial stretch of every segment is converted into discrete link lengths which, together with the derived twist and bend angles, depicts the achieved trajectory. Now, the objective function in Eq. 1 computes the weighted quadratic errors of the achieved solution compared to corresponding desired quantities of the target trajectory until the error is minimized for a given set of design parameters

condensed in a vector  $\underline{x}$ . The design parameter vector  $\underline{x}$  here comprises the actuation pressures for every configuration, the fiber angle and the length for every actuator segment and the initial bend angle for flexing and counter-flexing segments. In contrast to the original optimization algorithm  $^9$ , the weights are not prescribed by user preference. Here, the weights are evaluated following a deviate-based weighting scheme, that is, the weights are determined according to the deviation in the input variables (see Supplementary Materials). Further, an inequality constraint was applied, so that each design parameter is restricted by an individual permitted range which incorporates the manufacturability of the whole actuator.

#### Finite element modeling of actuators

In order to calibrate crucial analytical model parameters, we conducted finite element simulations of single pre-curved flexing and counter-flexing actuators with a constant length of l = 160mm using the commercial FEA software Abagus (SIMULIA, Providence, RI, USA). In all cases, the actuator was fixed at one end and a pressure was applied on its fluidic cavity linearly increasing up to a predefined value within a duration of 1s. We performed one simulation to determine the neutral axis for flexing and counter-flexing, respectively. Both models yielded fiber angles of  $\alpha = \pm 5^{\circ}$  and initial bend angles of  $\psi^{(0)} = 180^{\circ}$ . In order to draw conclusions on the location of the neutral axis in the circumference, sets of nodes on the outer surface along the actuator axis were defined at  $\varphi = \{0, 25, 35, 45, 90, 180\}^{\circ}$  and  $\varphi = \{0, 25, 35, 45, 90, 180\}^{\circ}$ {0, 90, 130, 150, 160, 180}° for flexing and counter-flexing respectively and their corresponding strain in the deformed state was computed. As already stated by Connolly et al., our extension of the analytical flexing model is defined under the assumption of thin cylindrical walls and therefore behaves stiffer than the FEA counterpart for experimentally derived model parameters. This way, we fit effective model parameters on the basis of a set of simulations of single precurved flexing and counter-flexing actuators with fixed initial bend angles of  $\psi^{(0)} = 180^{\circ}$ . The calibration procedure was evaluated by a nonlinear least-squares algorithm which minimized the error between deformed bend angles derived by FEA and the corresponding analytical solution. Subsequently, the optimized parameter set was validated on additional numerical models which yielded constant fiber angles of  $\alpha = \pm 5^{\circ}$  but varied in their initial bend angles of  $\psi^{(0)} =$  $\{0, 60, 120, 180\}^{\circ}$  and  $\psi^{(0)} = \{180, 210, 240, 270\}^{\circ}$  for flexing and counter-flexing actuators, respectively.

#### **Actuator fabrication**

After the actuator design parameters are output from the optimization, a computer aided design software (SolidWorks, Dassault Systèmes SE) is used to model the prescribed actuator and the molds that are 3D-printed in order to fabricate the actuator. When generating the model of the actuator, the fibers are modeled as swept grooves into the body of actuator, so that the fabricated elastomer body has precise guides to control the fiber orientation and placement. The fibers along pre-curved segments are initiated at the  $\varphi=0^\circ$  point at one end of the segment. Molds are printed on an Objet30 Prime 3D printer (Stratasys, Ltd., Prairie, MN, USA), preferentially in VeroClear (Stratasys, Ltd., Prairie, MN, USA). They are lubricated with Ease Release 200 (Smooth-On, Inc, Macungie, PA, USA).

Multi-material actuators are cast in a multi-step process. For our actuators, the less stiff material is DragonSkin 10 Medium (Smooth-On, Inc, Macungie, PA, USA) and the stiffer material is Smooth-Sil 950 (Smooth-On, Inc, Macungie, PA, USA). Silicone is mixed in a planetary

centrifugal mixer (THINKY MIXER, ARE-310, THINKY, Corp., Japan) for 30s at 2000rpm and then 30s at 2200rpm. The dominant material for an actuator, most often the less stiff one, is cast first. Further information on the silicone casting can be found in the Supplementary Materials, see Fig S4. After the first portion is cured (according to manufacturer's cure time at room temperature), excess silicone at the jointing surface is removed via a sharp knife, revealing a fresh silicone edge. Shortly afterwards, the second material, often the stiffer material, is poured into the appropriate portions of the mold. After the actuator is fully cured, the elastomer body plus inner core is demolded. A stiff wire is run between the inner core of the mold to separate the elastomer body from the inner core, but the inner core is not yet removed. Isopropyl alcohol, (Sigma-Aldrich, Inc, St. Louis, MO, USA) is used to lubricate the demolding process. With the inner core still inside the elastomer body, Kevlar fibers (McMaster-Carr, Elmhurst IL, USA) are hand-wound along the guiding marks around the elastomer body. The inner core is released and the ends are capped and sealed with Sil-Poxy (Smooth-On,Inc, Macungie, PA, USA). A vented screw is installed in the cured Sil-Poxy cap end at which the actuator will be pressurized from.

#### **Actuation validation experiments**

The experimental platform consists of a frame with adjustable elements coupling together a camera mount, a custom actuator mount, and a black sheet for the background. The actuators were fixed horizontally on the specific mount, so that the plane of bending is parallel to the ground in order to decrease effects of gravity on the bend angle. The actuators were pneumatically actuated via an electropneumatic custom control box. The videos were analyzed via a MATLAB script (MathWorks, Natick, MA, USA) to extract the enclosed bend angle, allowing comparison of the experimental results with the expected results from the optimization.

To obtain a richer level of data regarding the actuator deformation, a digital image correlation (DIC) process was also devised. DIC is an extremely versatile method of achieving non-contact full field strain maps on deformation bodies, and utilizes a speckle pattern and speckle tracking software. When a stereoscopic approach is employed utilizing two cameras, a three-dimensional strain evaluation is possible, revealing not only the strain field, but also rigid body displacement and out-of-plane displacement. The actuators were patterned first with a solid white base coat, followed by a random black speckle. High-speed videos of deformation were recorded. The strain and displacement output from discrete data points were then extracted to positionally match the output from the corresponding FE simulation.

Further details on the instrumentation used for actuator validation experiments are available in the Supplementary Materials.

# Simulated trajectory testing

For each case (opening and closing trajectories), we generated 28-sets of random trajectory input parameters. The random trajectories adhere to the following constraints:

(1) The first configuration parameters were generated using the uniform random generator function (rand) in MATLAB within the following bounds:  $\psi^{(1)} \in [0, \pi]$ ,  $l_{link,1}^{(1)}$ ,  $l_{link,2}^{(1)} \in [32.8 \text{mm}, 100 \text{mm}]$ .

- (2) Within one trajectory set of parameters, the bend angle may only undergo increases  $(\psi_1 \leq \psi_2 \leq \psi_3 \leq \psi_4)$  or decreases  $(\psi_1 \geq \psi_2 \geq \psi_3 \geq \psi_4)$ , and the link length segments may only increase  $(l_1 \leq l_2 \leq l_3 \leq l_4)$ . Because the trajectories were constrained to only allow for motions that can be accomplished via initially straight actuators, no trajectories were allowed to cross  $\psi = 0$ .
- (3) The final configuration parameters are generated using the uniform random generator function (rand) in MATLAB within the following bounds:  $\psi^{(4)} \in \{\psi^{(4)}: \psi^{(4)} > 0 \cap [\psi^{(1)} 79.7^{\circ}, \psi^{(1)} + 79.7^{\circ}]\}$ ,  $l_{link,1}^{(4)}, l_{link,2}^{(4)} \in [l_{link,1}^{(1)}, 1.289 \times l_{link,1}^{(1)}]$ . The 79.7° change in  $\psi$  is derived for the maximum change in psi for an initially straight flexing segment with a length of 20mm. The 28.9% length increase is chosen via calculating the maximum extending deformation at 100kPa for an actuator with  $\alpha = \pm 5^{\circ}$ .
- (4) The two intermediate configurations are randomly spaced (rand) between the selected  $l_{link,1}^{(1)}$  and  $l_{link,2}^{(4)}$ ,  $l_{link,2}^{(1)}$  and  $l_{link,2}^{(4)}$ , and  $\psi^{(1)}$  and  $\psi^{(4)}$ .

We calculated input-output errors for each link length and bend angle of each configuration of each trajectory-set. We combined the data sets of the closing and opening trajectories (n=56) and use the prescribed output pressures from these trajectories, to calculate pressure range utilization values and pneumatic surplus values. Data sets were not normally distributed according to a Kolmogorov-Smirnov test. The non-parametric Wilcoxon signed-rank test was used as the most appropriate paired difference test.

#### **Results**

# Model validation of pre-curved segments

Inclusion of pre-curved segments into the optimization algorithm requires updates to the analytical solution. In order to validate that the derived analytical solution will accurately correspond with the physical actuator behavior, we first consider the case of a pre-curved actuator consisting only of a single bending segment with a uniform  $\psi^{(0)}$ . The kinematics are derived by evaluating the equilibrium of moments around the neutral bending axis on the capped, unfixed end of the actuator, as previously described  $^9$ . The balance of moments is expressed as the comparison of the resulting force due to the internal pressure acting on the cap and the material response of the semi-cylindrical layers made of the two types of elastomers. We approximate the deformation at the capped end based on the well-known kinematics of the inflation-extension-torsion problem of anisotropic tubes  $^{13,14}$  and further assume there is no radial expansion  $\frac{r}{R}=1$  and causing the radial stress component to vanish,  $\sigma_{rr}=0$ . We design these actuators with an axially symmetric set of fiber wrappings so the actuator should experience no twisting,  $\tau=0$ . Consequently, the deformation gradient and the left Cauchy-Green deformation tensor reads as follows:

$$\underline{\underline{F}} = \begin{bmatrix} \lambda_z^{-1} & 0 & 0 \\ 0 & 1 & 0 \\ 0 & 0 & \lambda_z \end{bmatrix} \tag{2}$$

$$\underline{\underline{b}} = \begin{bmatrix} \lambda_z^{-2} & 0 & 0 \\ 0 & 1 & 0 \\ 0 & 0 & \lambda_z^2 \end{bmatrix} \tag{3}$$

This displays the dependence solely in axial stretch,  $\lambda_z$ , due to bending. In this model, the curvature in the bent configuration is constant across the whole actuator segment and the cross-sections are assumed to remain perpendicular along the actuator axis. In contrast to initially-straight bending actuators, material lines parallel to the actuator axis along the whole body of pre-curved actuators are not uniform in length with varying  $\varphi$ . In this way, a flexing or counterflexing actuator is, in addition to the initial bend angle  $\psi^{(0)}$ , characterized by its length measured on the outermost material line along circumferential angle  $\varphi=180^\circ$  within the cross-section. Using this information, we formulate a generalized axial stretch of a cylinder due to bending (in flexion or counter-flexion) of an arbitrary point in the cross-sectional plane:

$$\lambda_z = \frac{l - \psi^{(0)} R_o (1 + \cos(\bar{\varphi})) + \psi(R_o \cos(\bar{\varphi}) - R \cos(\varphi))}{l - \psi^{(0)} (R_o + R \cos(\varphi))} \tag{4}$$

Here,  $\psi^{(0)}$  and  $\psi$  are the undeformed and deformed bend angles;  $\varphi$  and R are the circumferential coordinate and the radius within the constraints  $0^{\circ} \leq \varphi \leq 180^{\circ}$  and  $R_i \leq R \leq R_o$  respectively; l is the actuator segment length; and  $\bar{\varphi}$  is the location of the neutral axis (dependent on subcategorization into flexion vs counter-flexion as seen in Fig 1B). The neutral axis is derived from FEA; it exists at  $\bar{\varphi}=35^{\circ}$  for flexing and at  $\bar{\varphi}=150^{\circ}$  for counter-flexing actuators, see Supplementary Materials for additional information. Using this expression for axial stretch together with the assumption of an isotropic, incompressible Neo-Hookean strain energy density for the elastomer layers and a linear elastic material behavior for the fiber reinforcements as in (14), we can derive the moment around the neutral axis that originates from the material response acting against the internal pressurization as follows:

$$M_{mat}(\psi) = 2 \int_{0}^{\pi} \int_{R_i}^{R_o} \sigma_{zz} \lambda_z^{-1} R(R_o \cos(\bar{\varphi}) - R \cos(\varphi)) dR d\varphi$$
 (5)

The opposing moment around the neutral axis as a consequence of the applied pressure is given by:

$$M_{cap}(P) = 2PR_i^2 \int_0^{\pi} \sin(\varphi)^2 \left( R_o \cos(\bar{\varphi}) - R_i \cos(\varphi) \right) d\varphi \tag{6}$$

Finally, our objective function evaluates the equilibrium of moments about the neutral axis to solve for the required pressure to achieve a desired bend angle via:

$$f_{EoM}(\psi, P) = M_{mat}(\psi) - M_{cap}(P) = 0$$
 (7)

For further details of this derivation see Supplementary Materials and Fig. S2.

Although finite element analysis (FEA) generally provides more accurate predictions than an analytical bending model, it is far more computationally expensive. Thus, by creating an

optimization algorithm that depends on a robust analytical model instead of FEA, the optimization process improves the actuator design workflow.

In order to increase the general validity of the model, we analogously performed FEA simulations for flexing and counter-flexing actuators which exhibit a constant length of  $l=160\,\mathrm{mm}$  and constant fiber angle  $\alpha=5^\circ$ , but vary in their initial bend angles of  $\psi^{(0)}$ . (Validation of accuracy for other parameters included in Supplementary Materials, see Fig. S3). We ran FEA on select cases in order to validate our analytical solution, enabling us to proceed with the preferable, less computationally expensive option while also maintaining confidence in the accuracy of the analytical predictions. The analytical model demonstrates generally low relative error values. The analytical model shows relative deviations from the FEA results in the range of  $2.72\pm0.77\%$  (Fig. 2A) for the flexing actuators and  $5.27\pm8.6\%$  (Fig. 2B) for the counterflexing actuators. The FEA predicted conformation at 27.6kPa is shown for the flexing (Fig. 2C) and counter-flexing (Fig. 2D) actuators. In summary, the parameter optimization offers comparable results to FEA predictions and therefore generalizes the computational validity of the analytical model for varying model parameters.

Subsequently, the analytical and finite element models were further validated with experimental data collected from physical prototypes, seen in Fig. 3. Physical actuator performance was evaluated on three prototypes for flexing actuators and two counter-flexing actuators with length l=160mm, fiber angles  $\alpha=\pm 5^\circ$  and initial bend of  $\psi^{(0)}=180^\circ$  via two methods; optical tracking of the bend angle, and digital image correlation (DIC) to track the displacement of points along the actuator.

In order to compare the bend angle to the analytical predictions, flexing actuators were pneumatically activated by iteratively increasing pressures of up to 27.6kPa in 3.4kPa (0.5 psi) steps. The maximum pressure was constrained based on FEA predictions depicting a 360° bend angle at 37kPa, in which the actuator would bend into a full circle and thus the free end would collide into the fixed end of the actuator. Counter-flexing actuators were tested in 6.9kPa (1 psi) steps until a maximum pressure of 48.3kPa (7 psi). Upon every pressure step, the valve was closed after the corresponding nominal pressure was reached and opened after the actuator occupied its steady state response. The video data was analyzed using a representative frame for each pressure step, from which the steady-state deformed bend angle was extracted. The comparison of the analytical model with the experimental results from the optical tracking is shown in Fig. 3A for a flexing actuator and in Fig. 3B for a counter-flexing actuator. The representative video frame at 27.6kPa is shown in Fig. 3C for a flexing actuator and in Fig. 3D for a counter-flexing actuator. One limitation of this comparison is that fabrication errors can be seen in the deviation from the prescribed ideal initial bend angle for the unpressurized configuration and the inter-actuator variability at equivalent pressures. For flexing actuators, the analytical model predicted larger changes in bend angles than the physical prototypes. This is concordant with the previous results of the optimization work 9, in which Connolly et al. observed this phenomenon for their initially straight bending actuators yielding low fiber angles. We assume that gravitational effects decrease the change in curvature for physical actuators and therefore, the analytical model might be seen as an idealization of the real system, since it neglects body forces and effects of inertia. Another potential source of error is gravity's effects on the consistency and accuracy of the testing method. The bending curvature of an actuator

could be out of plane, so that it appears slightly twisted around its curved axis and subsequently yields lower than expected changes in its bend angles for flexing and counter-flexing. Body forces such as gravity highly depend on the volume it affects. Shorter segments of actuators decrease these negative effects on actuator performance and, simultaneously, increase the accuracy of the analytical prediction; aiming for shorter segments is beneficial for the optimization of segmented actuator design presented in the rest of this manuscript.

We conducted an additional experimental method to validate the FEA model via DIC to quantify the net in-plane displacement of various points along the physical actuator. By measuring displacement of the actuator, we reduce the influence of the manufacturing error in which the initial bend angle has slight variations from the exact prescribed initial bend angle. We compare the FEA predicted displacement of four select points along the  $\varphi = 90^{\circ}$  material line of the actuator to the DIC derived displacement for the flexing (Fig. 3E) and counter-flexing (Fig. 3F) actuators with an initial bend angle of  $\psi^{(0)} = 180^{\circ}$ . The flexing actuator does continue to show the trend of being stiffer than predicted. We generally observe good matching of the displacement between the DIC and FEA data, and we specifically see excellent matching for the case of the counter-flexing actuators. The displacement heat map derived from DIC showing the flexing (Fig. 3G) and counter-flexing (Fig. 3H) actuator pressurized to 27.6kPa can also be visually compared to the FEA frame in Fig. 2C and D, respectively. One limitation of the DIC is that due to the curvature of the actuator, the software has trouble analyzing the edges and cannot capture data for these curved sides. With that said, we see robust qualitative matching between the heat maps plotted with the same heat scale of 2C,D and 3G,H, even without the capture of the edge effects. By cross-validating between the analytical model, the FEA, and experimental methods, we can confidently proceed with our analytical model.

# Increased fidelity of optimization outputs

The introduction of a new decision variable,  $\psi^{(0)}$ , allows for the optimization to achieve more accurate outputs that have higher fidelity to the input trajectories. In order to investigate the increase in accuracy conferred by the inclusion of pre-curved segments, we tested the optimization software with sets of randomly generated input trajectories. For our simulated trajectory testing, we assume the case of a two-link input trajectory, in which each motion trajectory is composed of 4 discrete configurations (j=4). This assumed trajectory format is consistent with the format of the biological diaphragm motion data we use later. It is assumed that the configurations are temporally ordered, but the pressure to achieve the first configuration  $(P_1)$  is not necessarily the lowest nor highest pressure. Two cases of trajectory data were tested, the case of an opening angle trajectory ( $\frac{d\psi}{dt} < 0$ ) and the case of a closing angle trajectory ( $\frac{d\psi}{dt} > 0$ ). For each case, we generated 28 sets of random input trajectory data with four configurations per trajectory. The trajectory inputs were constrained to only cases that an initially straight actuator could generate—therefore trajectories that crossed  $\psi = 0$  were excluded (see Materials and Methods for more information). Each set of input data was run through the optimization algorithm both with the pre-curved segment capability  $(\psi^{(0)} \in [0,\pi])$  and with initially straight actuators ( $\psi^{(0)} = 0$ ). The output trajectories were calculated based on the optimized parameters, and the output link lengths and bend angles were compared to the corresponding input link lengths and bend angles. The percent errors are shown in Fig. 4. Due to the high prevalence of extreme values such as the 800% error point seen in Fig. 4B, the data is not normally distributed and a non-parametric test is used to compare them.

In Fig. 4A, for an opening angle trajectory, the median percent error of the output bend angles derived from the parameters specified by the algorithm is 0.83% for initially straight actuators and 0.61% for pre-curved actuators. We find more substantial accuracy savings in Fig. 4B when we consider opening angle trajectories; the median percent error is 4.0% for initially straight actuators and is 0.77% for pre-curved actuators. The accuracy savings are greater in link lengths than in the bend angles, which is largely influenced by how the weighting scheme in the optimization function distributes errors for the cases of initially straight actuators. For link length errors for closing trajectories, the median percent error is 14% for initially straight actuators and 0.89% for pre-curved actuators, see Fig. 4C. Similarly, for link length errors of closing trajectories, the median percent error is 15% for initially straight actuators and 0.66% for pre-curved actuators, see Fig. 4D. Manual adjustment of the weights for the initially straight actuators could lead to a more even distribution of error. Overall, we find that the deviate-based weighting provides for sufficiently small errors between the desired input trajectory and the optimized expected output trajectory.

The median percent-error for the pre-curved actuators is under 1% in all four avenues of data. The uniformity of the distribution of error in the case of pre-curved actuators indicates that the weighting scheme is appropriate for the optimization. It is notable that the initially straight actuators also have more extreme outliers in the data, indicating that the optimization with the pre-curved segment capability allows for a more robust handling of various input trajectories.

# Replication of complex bioinspired bending motion

The inclusion of pre-curved segments into our optimization algorithm enables us to mimic the initially curved states of many complex biological systems in nature. As a demonstration of this technology, we sought to replicate two examples of complex bending motion derived from biology, the domed motion of the diaphragm <sup>11,15</sup> and the contractile bell propulsion of a jellyfish. <sup>12</sup> Specifically, we look at replicating the coronal and sagittal plane motion of the right hemisphere and the cross-sectional deformation of a jellyfish's bell. The input trajectory data was sourced from existing literature. 12,15 For the diaphragm especially, the introduction of precurved actuators is critical, because an initially straight resting configuration is unrealistic for the muscle fibers of the diaphragm. The workflow of taking input biological data and converting it to an actuator is seen in Fig. 1. First, we extract the relevant trajectory points that we aim to mimic. For the case of the diaphragm, the input data is derived from cine magnetic resonance images (MRI) from pre-existing respiratory imaging studies. <sup>15</sup> This MRI data is available for the coronal plane imaged at the plane through the tracheal bifurcation and the sagittal plane imaged through the right midclavicular line. We aim to replicate the motion of the diaphragm muscle found in these planes of imaging. We opt to focus on the data for the motion of the right hemisphere because the beating of the heart distorts motion tracking efforts for the left hemisphere; we make a simplification that assumes left-sided symmetry to the right sided diaphragm motion to best represent the intrinsic motion of the diaphragm muscle. As the native muscle fibers in the diaphragm anchor to the central tendon, <sup>16,17</sup> we opt to track a trajectory that follows the lateral side of the diaphragm to the peak of the diaphragm curvature, assuming that this is where the fibers anchor to the central tendon. We assume no contractile motion within the central tendon. From this, we extract the input trajectory shown in Fig. 5A from video frames at four time points along a single exhalation cycle. These trajectories are input into the optimization software, which subsequently outputs the fabrication and actuation parameters to best match these four

configurations pulled from the biological data. The optimization predicts the actuator conformations shown in Fig. 5B. The optimization aims to match the outer edge of the actuator (the material line along  $\varphi=180^\circ$ ) to the input trajectory (the curvature of the diaphragm). Although there is some discrepancy, we see that the qualitative error largely derives from differences in the desired link length, especially link length 1. If greater link length fidelity is desired, the weights can be manually adjusted.

Given the output parameters, we fabricate the actuators according to the workflow described in Fig. 1E. The actuators are mounted onto an acrylic stand via the actuator base and pneumatically actuated using a control system that relies on electropneumatic regulators. Using a video tracking script (MATLAB), we select representative frames of the actuator in a steady state when pressurized to each of the specified pressures and compare the conformation to the expected analytical solution, see Fig. 5C. In order to actuate the system to replicate the dynamic motion that the input trajectories derive from, the specified pressures are plotted with the time point of their respective video frames. The conformations between the time points will be generated via a linear interpolation between the specified pressures (P<sup>(1)</sup>, P<sup>(2)</sup>, P<sup>(3)</sup>, and P<sup>(4)</sup>), as seen in the pneumatic control scheme in Fig. 5D.

The link lengths yield larger error values than bend angles (maximum deviation of 0.13%). The error in link lengths depict an asymmetrical distribution with a corresponding median of 0.79%, as seen in Fig. 5E. Since this value is sufficiently small and the associated maximum error of 4.1% is still below a 5% threshold and we see good qualitative matching in Fig. 5B, we declare the analytical model with the underlying set of optimized design parameters as a good approximation with respect to the desired, discrete input trajectory. In Fig. 5C, the fabricated actuators demonstrate very good fidelity to their analytically predicted conformations; in fact, they show better fidelity than what is seen in the single-segment actuators investigated in Fig. 3. This is largely due to the shorter segment lengths of the pre-curved actuators, here they are on the order of 40-70mm compared to 160mm in the example actuator investigated earlier. The analytical solution represented by the predicted actuator outline depicts excellent agreement with the corresponding outline of the physical actuator throughout all configurations and consequently highlights the accuracy of the calibrated analytical model for reproducing the physical actuator behavior upon pressurization.

To build a biomimetic soft robotic jellyfish, a similar process is employed. We opt to track the contractile motion data that is extracted from Villanueva et al. 12, Fig. 6A. The bell of a jellyfish in a relaxed state is slightly domed and the dome further curls upon movement. Thus, our precurved actuators that flex are appropriate for the replication of such motion. Radial symmetry of the bell of the jellyfish is assumed, and existing cross-sectional analysis 12 is used to derive an input trajectory for the optimization, as seen in Fig. 6A-D. The tracking trajectories for both of these biological applications are derived from planar data, and the actuators can be oriented together in their 3-dimensional context in order to replicate these motions fully. A silicone connector is used to couple four actuators together radially, so they share a single fluidic cavity, as seen in Fig. 6E. A glow-in-the-dark, UV-reactive silicone sheet molded to a dome shape is stretched over the complex of four actuators to form the bell of the jellyfish. This soft robotic jellyfish can be actuated with the control scheme in Fig. 6B to generate the contractile motion of the jellyfish, seen in Fig. 6F and Movie S2. Because the analytical model and the optimization do

not consider body forces, we find that when actuated with air in water, the buoyancy and water resistance require the system to be actuated at higher pressures than prescribed to achieve the same motion. Because the forces in any given biological system are system dependent, this model should be updated on an application-dependent basis to consider the relevant that the actuators will encounter.

#### Pneumatic efficiency enabled by pre-curved actuators

By fabricating the actuators with a pre-curved configuration, the unused range of motion—indicative of an inefficient system—required to reach the first configuration from a straight cylinder is eliminated. The inclusion of pre-curved actuator segments in the optimization algorithm allows for more pneumatically efficient and more accurate replication of complex bending motion. Fluidic soft actuator systems often rely on pneumatic regulators to provide accurate and precise control. When soft actuator systems demand high operating pressures and high precision regulators, the costs of the control system rapidly increase due to the precision engineering required to create such instrumentation. The creation of pneumatically efficient actuators relieves the requirements of a pneumatic system, allowing for the use of lower-cost control systems.

Pneumatic efficiency can be quantified via two metrics: pressure range utilization (PRU) and the pneumatic surplus value (PSV). PRU is quantified as the pneumatic range normalized to the maximum prescribed pressure via:

$$PRU = \frac{\text{range}(P^{(1)}, ..., P^{(j)})}{\max(P^{(1)}, ..., P^{(j)})}$$
(8)

In which a PRU value of one indicates a fully utilized system, and a PRU value close to zero indicates a poorly utilized system where the prescribed pressures to achieve the input configurations cluster at the maximum end of the pressure range. A poorly utilized system reflects the amount of "wasted" pneumatic work in order to achieve the conformation that exists at the lowest pressure. PRU yields a metric that can capture the unused pressure range.

Pneumatic surplus is quantified as the minimum prescribed step size in between any two configurations normalized to the minimum step size of a given pneumatic regulator via:

$$PSV = \frac{\min\left(\operatorname{abs}(P^{(j)} - P^{(j-1)}, \dots, P^{(2)} - P^{(1)})\right)}{\operatorname{minimum regulator step size}}$$
(9)

A pneumatic surplus value (PSV) less than one indicates that the given pneumatic regulator is insufficient in its precision and is unable to achieve differentiable configurations for a given actuator. For our testing, we utilize SMC ITV1000 series electropneumatic regulators (SMC Corporation, Chiyoda, Tokyo, Japan) which have a minimum output unit of 0.7kPa (0.1psi). A PSV much greater than one indicates the surplus capacity of the pneumatic system, indicating the degree to which the actuator can suffice with a less precise, and thus less costly, pneumatic regulator.

Using the randomly generated trajectory data from earlier, we can extract the PRU and pneumatic surplus from a pool of 56 sets of trajectory data comparing the initially straight actuators with the pre-curved actuators, seen in Fig. 7A. The pre-curved actuators have a median value of 1 compared to the initially straight actuators with a median PRU of 0.26, indicating that the initially straight actuators have a tendency to waste three-fourths of their pressure range to achieve the lowest pressure conformation. The pre-curved actuators have a median PSV of 13 compared to the initially straight actuators median PSV of 3.2. The average pre-curved actuator can suffice with a pneumatic regulator that is 4-fold less precise to achieve the same resolution as the initially straight actuators.

To investigate the effect of the inclusion of pre-curved actuator segments in the setting of replicating biologically derived motion, three sets of input trajectories were studied for the case of diaphragm motion. From the clinical MRI data in the coronal and sagittal planes, the muscle fiber trajectory of the diaphragm—which anchors from the ribcage to the central tendon  $^{11,15,17}$ —is extracted from the right hemidiaphragm over an exhalation cycle, as seen in Fig. 7B. The muscle fiber trajectory from the sagittal plane is broken into two trajectories, an anterior and posterior segment. The three input trajectories—derived from the motion in the coronal plane, the anterior half of the sagittal plane, and the posterior half of the sagittal plane—were input into the optimization algorithm with the imposed boundary conditions of  $\psi^{(0)} = 0$  or  $\psi^{(0)} \in [0, \pi]$ , an initially straight actuator or pre-curved actuator respectively. The resulting pneumatic control scheme for these three cases are plotted in Fig. 7C, in which each specified pressure ( $P^{(1)}$ ,  $P^{(2)}$ ,  $P^{(3)}$ , and  $P^{(4)}$ ) is plotted, with the color directionality indicating the direction of the ordered progression from  $P^{(1)}$  to  $P^{(4)}$ .

For all three input trajectories, the pre-curved actuators consistently have lower maximum pressures, wider pressure ranges between P<sup>(1)</sup> to P<sup>(4)</sup>, and wider step sizes between pressures. The greatest change in required maximum pressure is seen for the input trajectory derived from the anterior half of the sagittal plane, in which the initially straight actuator demands a maximum pressure of 74.7 kPa whereas the pre-curved actuator demands a maximum pressure of 33.3 kPa—a 55% reduction. The greatest change in utilization of the pneumatic range occurs for the input data that is extracted from the posterior half of the sagittal plane, in which the pneumatic range shifts from 59.9-69.5kPa with a PRU of 0.14 for the initially straight actuator to 0-65.0 kPa with a PRU of 1 for the pre-curved actuator. The pneumatic range widened by 570%. The smallest pressure step sizes are required by the initially straight actuators for the sagittal posterior input motion and coronal plane input motion—the smallest required step sizes are 0.01 kPa (0.01) and 0.24kPa (PSV of 0.4) respectively for the pressure difference between P<sub>3</sub> and P<sub>4</sub> (step sizes are not visible on the chart). The PSVs of less than one indicate that these step sizes are actually below the resolution of the minimum 0.7kPa step size of the SMC ITV1000 series electropneumatic regulators which we have used for previous work <sup>18</sup>. For these same input trajectories, the pre-curved actuators have a smallest required step size of 4.6kPa (PSV of 6.6) and 1.5kPa (PSV of 2.1), respectively. The initially straight set of actuators prescribed by the optimization algorithm requires a more precise pneumatic regulator with higher pressure capacity in order to generate the expected conformations.

As discussed earlier, there is a degree of inherent error when we must reconcile different actuator segment behavior that is generated by one shared fluidic cavity and uniform pressure in all

segments. The optimized solution thus represents the parameters that generate a minimum overall error. When the link lengths and bend angles of expected conformation from the analytical solution are compared with the input trajectory, see Fig. 7D, pre-curved actuators not only utilize a more pneumatically efficient actuation control scheme, but also, have more accurate conformations with respect to the desired input trajectory. The pre-curved actuators for our biological examples are all an order of magnitude more accurate in terms of percent error than the initially straight actuators (Fig. 7D), which is consistent with our generalized findings from Fig. 4. As link length is a better representative of the diaphragm muscle function, the more accurate link length of the pre-curved actuators are better mimics of the biological diaphragm function than the initially straight actuators. These errors can be qualitatively seen in the visualization of the actuators generated for a coronal plane input trajectory in Fig. 7E, in which the outer edge (the material line along  $\varphi = 180^{\circ}$ ) intends to follow the curvature of the diaphragm. The high link length error for the initially straight actuators results in a fiberreinforced actuator that sits fully beyond the diaphragm in the red highlighted lung region; this effect is especially apparent in the configuration 1 state. Overall, pre-curved actuators enable more pneumatically efficient and more accurate generation of biomimetic fiber-reinforced actuators compared to their initially straight counterparts.

#### Conclusion

In order to achieve high fidelity biomimicry using fiber reinforced actuators, we need a technological update to facilitate the translation of these programmable soft robotic actuators. By reframing the analytical solution to include this new decision variable, the resting bend angle  $\psi^{(0)}$ , we unleash a wide berth of capabilities in the optimization algorithm. When we compare the optimization results for a set of input trajectories that can be achieved by both pre-curved and initially straight actuators, we find that the optimization is both more accurate and more robust in replicating biological input data with pre-curved actuators. Pre-curved actuators also enable the creation of actuator motions that are previously unachievable. By enabling a pre-curved fabrication, we can introduce the capability of capturing "opening" angles via material orientation to utilize counter-flexing actuator segments. With initially straight actuators, "opening" motions  $(\frac{d\psi}{dt} < 0)$  are achieved via using the maximum pressure to achieve configuration one, and relaxing the actuator pressurization  $(\frac{dP}{dt} < 0)$  to create subsequent configurations because they can only utilize flexing segments  $(\frac{d\psi}{dP} > 0)$ . Pre-curved actuators remove this restriction, and can achieve opening motions via either pressurization scheme ( $\frac{dP}{dt}$  < 0) or ( $\frac{dP}{dt}$  > 0) which allows for the freedom to adjust the actuation scheme of the actuator to the analogous biological actuation of the input data. Additionally, pre-curved counter-flexing actuators can generate bending motions that cross the  $\psi = 0$  point—such as an actuator with an initial configuration of  $\psi = 180^{\circ}$  that straightens to  $\psi = 0$  and then continues past this to a final configuration of  $\psi = -180^{\circ}$ —creating what appears to be first "opening" then "closing motion". This is a motion trajectory that is commonly found in biology—such as the wrist moving from a flexion position to a hyperextension position—that is impossible to achieve with the initially straight actuators. For some complex biological geometries such as the diaphragm, an initially straight configuration is entirely unrealistic, and thus the introduction of pre-curved actuators is a foundational improvement to create a biomimetic system of the diaphragm. We demonstrate the robustness of application of this technology via application to two biological systems, the human diaphragm and the bell of a jellyfish. As we use data from planar crosssectional motion for these applications, we can orient these representations of motion in 3D-space in an arrangement derived from their planar orientations to generate full-bodied 3D complex bending motions.

Further, pre-curved actuators enable the concept of pneumatic efficiency, which facilitates the usage of less powerful and/or less precise pneumatic controls, and thus less expensive instrumentation. This is necessary for the translation of biomimetic actuators into widely used technology. For pneumatic regulator equipment, economic cost scales with higher power and higher precision. Pneumatically efficient actuators decrease the final instrumentation costs of the control system required to operate these soft robotic systems. Decreasing the hardware costs and complexity is a key step in translating these soft robotic actuators to full utilization.

This work is limited by the fabrication complexity, as this technology update trades ease of fabrication for accurate bending motion replication and pneumatic efficiency, the approach would be greatly aided by innovations in multi-material manufacturing methods. A key limitation is that the current mode of fabrication is costly in both manual time and curing time, leading to long start-to-finish manufacturing time (on the order of days). A high-throughput automated but customizable manufacturing method for these multi-moduli actuators would greatly aid the application and utilization of these actuators. We also noticed age-related changes in the actuators, with actuators fabricated approximately a year ago behaving much stiffer than more recently fabricated actuators. The analytical model can easily change out the material model, so one could easily run the optimization with aged silicone parameters. Measures could also be taken to slow aging effects, such as cryogenic storage. With that said, age effects are an inherent material-based problem that would benefit from thorough characterization or advancements in materials science.

As fiber-reinforced actuators rely on pneumatic controls, we opt to actuate them using tethered systems to electropneumatic regulators. In the pursuit of tether-free soft-robotics, the pneumatic efficiency conferred by pre-curved actuators may allow for an actuator to function at the lower pressure capabilities required by tether-free systems.

Further optimization of the system could include adding force exertion of the actuator as an input parameter. Such an update would require an analytical solution for a specified force vector such as an effector normal force exerted by the cap. As our baseline analytical solution does not consider body forces or external force environments, the optimization needs to be updated on an application specific basis. In such cases, the pressure/force requirements of the system will act as an additional constraint on the optimization. In order to accommodate the addition of constraints to an optimization, additional degrees of freedom to the system are not just beneficial, but necessary. The addition of  $\psi^{(0)}$  will be critical in developing an optimization that can generate actuators to follow native motions and forces.

Ultimately, pre-curved actuators can capture motions that initially straight actuators cannot, and are also more accurate, robust, and efficient for the motions that can be generated with initially straight actuators. They are better suited to capture the geometric complexity of biological actuators and systems. Pre-curved actuators function as an enabling technology for the creation of bioinspired robotic systems, such as an artificial diaphragm driving respiration or artificial

trunk that rotates about the spine. This work provides a robust and versatile platform to precisely translate complex *in vivo* motion into biomimetic soft robotic actuators.

# Acknowledgments

We acknowledge Jackson Hardin for his help with the video capture.

**Funding:** This work was supported, in part, by a Seed Grant from Muscular Dystrophy Canada, a Discovery Research Grant from the Muscular Dystrophy Association, and an NSF CAREER award #1847541. L.H. is the recipient of the Doctoral Foreign Study Award from the Canadian Institute of Health Research. **Author contributions:** L.H., D.G., J.N., and E.T.R designed the research. L.H. and D.G. designed and developed the fabrication process. D.G. designed the software updates. D. G. and Y.F conducted the finite element analysis. J. N. performed the digital image correlation testing. L.H. conducted the simulated trajectory testing. L.H. and D.G. designed and fabricated the diaphragm actuators. M.K. designed and fabricated the jellyfish. L.H., D.G., J.N., analyzed the data. L.H., D.G., J.N., G.M, and E.T.R. wrote the manuscript.

**Competing interests:** No conflicts of interest.

**Data and materials availability:** Biological motion data was sourced from the published works of Mankodi, et al <sup>15</sup> and Villanueva, et al <sup>12</sup>. Software code and actuators are available through a materials transfer agreement.

#### **References and Notes**

- 1. Kim S, Laschi C, Trimmer B. Soft Robotics: A Bioinspired Evolution in Robotics. Trends Biotechnol. 2013;31(5):287–294.
- 2. Hughes J, Culha U, Giardina F, Guenther F, Rosendo A, Iida F. Soft Manipulators and Grippers: A Review. Front. Robot. AI. 2016;369.
- 3. Frame J, Lopez N, Curet O, Engeberg ED. Thrust Force Characterization of Free-Swimming Soft Robotic Jellyfish. Bioinspir. Biomim. 2018;13(6):064001.
- 4. Paschal T, Bell MA, Sperry J, Sieniewicz S, Wood RJ, Weaver JC. Design, Fabrication, and Characterization of an Untethered Amphibious Sea Urchin-Inspired Robot. IEEE Robot. Autom. Lett. 2019;4(4):3348–3354.
- 5. Polygerinos P, Wang Z, Overvelde JTB, Galloway KC, Wood RJ, Bertoldi K, Walsh CJ. Modeling of Soft Fiber-Reinforced Bending Actuators. IEEE Trans. Robot. 2015;31(3):778–789.
- 6. Bishop-Moser J, Kota S. Design and Modeling of Generalized Fiber-Reinforced Pneumatic Soft Actuators. IEEE Trans. Robot. 2015;31(3):536–545.
- 7. Bishop-Moser J, Krishnan G, Kim C, Kota S. Design of Soft Robotic Actuators Using Fluid-Filled Fiber-Reinforced Elastomeric Enclosures in Parallel Combinations. IEEE Int. Conf. Intell. Robot. Syst. 2012;4264–4269.
- 8. Connolly F, Polygerinos P, Walsh CJ, Bertoldi K. Mechanical Programming of Soft Actuators by Varying Fiber Angle. Soft Robot. 2015;2(1):26–32.
- 9. Connolly F, Walsh CJ, Bertoldi K. Automatic Design of Fiber-Reinforced Soft Actuators for Trajectory Matching. Proc. Natl. Acad. Sci. 2017;114(1):51–56.
- 10. Hwang J, Knapik GG, Dufour JS, Marras WS. Curved Muscles in Biomechanical Models of the Spine: A Systematic Literature Review. Ergonomics. 2017;60(4):577–588.
- 11. De Troyer A, Boriek AM. Mechanics of the Respiratory Muscles. In *Comprehensive Physiology*; John Wiley & Sons, Inc.: Hoboken, NJ, USA, 2011; Vol. 1, pp. 1273–1300.
- 12. Villanueva AA, Priya S. Cyanea Capillata Bell Kinematics Analysis through Corrected In

- Situ Imaging and Modeling Using Strategic Discretization Techniques. PLoS One. 2014;9(12):e115220.
- 13. Goriely A, Tabor M. Rotation, Inversion and Perversion in Anisotropic Elastic Cylindrical Tubes and Membranes. Proc. R. Soc. A Math. Phys. Eng. Sci. 2013;469(2153):20130011–20130011.
- 14. Sedal A, Bruder D, Bishop-Moser J, Vasudevan R, Kota S. A Continuum Model for Fiber-Reinforced Soft Robot Actuators. J. Mech. Robot. 2018;10(2):024501.
- 15. Mankodi A, Kovacs W, Norato G, Hsieh N, Bandettini WP, Bishop CA, Shimellis H, Newbould RD, Kim E, Fischbeck KH, *et al.* Respiratory Magnetic Resonance Imaging Biomarkers in Duchenne Muscular Dystrophy. Ann. Clin. Transl. Neurol. 2017;4(9):655–662.
- 16. De Troyer A, Estenne M. Limitations of Measurement of Transdiaphragmatic Pressure in Detecting Diaphragmatic Weakness. Thorax. 1981;36169–174.
- 17. Whitelaw WA. Shape and Size of the Human Diaphragm in Vivo.
- 18. Roche ET, Horvath MA, Wamala I, Alazmani A, Song S-E, Whyte W, Machaidze Z, Payne CJ, Weaver JC, Fishbein G, *et al.* Soft Robotic Sleeve Supports Heart Function. Sci. Transl. Med. 2017;9(373):1–12.

### **Figure Captions**

- FIG. 1. Schematic of the introduction of pre-curved segments into the design optimization process. Fiber-reinforced actuators consist of an elastomer body with a fluid filled cavity that is wrapped in inextensible fibers (depicted in yellow). Extending and twisting segments consist of a single elastomer (white) body, whereas bending segments consist of a dual elastomer body (blue depicts the stiffer elastomer). (a) Pre-curved bending actuators can be subcategorized into flexing and counter-flexing actuators. (b) Schematic of material stress parallel to the body of the actuator ( $\sigma_{zz}$ ), defined in the cross-sectional plane. (c) Schematic of fiber angle ( $\alpha$ ) in relation to circumferential cross-sections of the actuator. (d) Schematic of updated optimization. (e) Fabrication schematic.
- FIG. 2. Validating the analytical model via finite element analysis. The predicted bend angle pressure response for the analytical model and finite-element model for varying  $\psi^{(0)}$  is compared for the (a) flexion and (b) counter-flexion case. The FEA deformation and strain results for specific actuators of outer length of 160mm and fiber angle of  $\alpha = \pm 5^{\circ}$  pressurized to 27.6kPa (4psi) is shown for the (c) flexion and (d) counter-flexion case.
- FIG. 3. Validating the analytical model and finite element analysis with experimental results. The experimental bend angle pressure response determined via optical tracking is compared to the analytical model for varying  $\psi^{(0)}$  for the (a) flexion and (b) counterflexion case. A representative image from the optical tracking image of bend angle for specific actuators of outer length of 160mm and fiber angle of  $\alpha=\pm 5^{\circ}$  pressurized to 27.6kPa (4psi) is shown for the (c) flexion and (d) counter-flexion case. The best fit arc is overlaid in red. The finite-element analysis predicted displacement is compared with the experimentally determined DIC displacement of four-discrete points for the (e) flexion and (f) counter-flexion case. The DIC image of displacement for specific actuators of

outer length of 160mm and fiber angle of  $\alpha = \pm 5^{\circ}$  pressurized to 27.6kPa (4psi) is shown for the (g) flexion and (h) counter-flexion case.

- FIG. 4. Accuracy of the optimization with the inclusion of an initial bend angle,  $\psi^{(0)}$ . The optimization software was tested with randomly generated input trajectories, in which we compare the resulting percent-error of the optimized output trajectory compared to the desired input trajectories. (a) Closing trajectory bend angle errors (p=0.02). (b) Opening trajectory bend angle errors (p=8×10<sup>-14</sup>). (c) Closing trajectory link length errors (p=8×10<sup>-38</sup>). (d) Closing trajectory link length errors (p=3×10<sup>-37</sup>). The cases of closing and opening trajectories are tested with 28 trajectory sets each. The bend angle data sets have n=112. The link length data sets have n=224. Boxplots show the interquartile range in blue and the median value in red. Data is compared with a Wilcoxon signed-rank test. \*p<0.05,\*\*p<0.01,\*\*\*p<0.001
- FIG. 5. Pre-curved actuators designed to follow diaphragmatic motion in exhalation. (a)

  The diaphragm muscle motion trajectory of the right hemidiaphragm from a coronal plane is extracted and discretized from the cine MRI of a healthy subject in maximal breathing, data modified from Mankodi et al<sup>15</sup>. Four frames across one exhalation motion are selected. (b) The expected configuration of the actuator at the prescribed pressures overlaid with a close up of the selected MRI frames. (c) The deformation of the fabricated actuator is compared to the analytically predicted trajectory from the optimization. (d) The pneumatic control scheme uses a linear interpolation between the specified pressures. (e) The error between the input trajectory parameters is compared with the analytically predicted link lengths and bend angles that result from the optimized actuator. Median shown in red. These actuators are dynamically compared to the input data in Movie S1.
- FIG. 6. Replicating planar motion with fiber reinforced actuators allows us to spatially couple actuators together to replicate 3-dimensional motion. (a) Motion trajectory data is extracted from previous kinematic analysis of a jellyfish bell during contraction, modified from Villanueva, et al <sup>12</sup>. (b) The output actuation pressures combined with the temporal data from the source kinematic analysis determine actuation parameters. Inlaid jellyfish stills modified from Villanueva, et al<sup>12</sup>. (c) The fabrication parameters and expected configuration of the actuator at the prescribed pressures are output from the optimization. (d) The analytically predicted solution is compared with the deformation of the fabricated actuator. (e) Four actuators are coupled together via a center connector, allowing them to share one fluidic cavity. The connector piece is shown with two actuators attached to show details of the connector. (f) 3-dimensional biomimetic softrobotic jellyfish by coupling the pneumatic actuators with a glow-in-the-dark silicone bell actuated in water. Frames taken from one cycle of pneumatic motion over a period of 3 seconds. Frames in this figure are rotated 90 degrees to orient the jellyfish motion upwards for visualization. The jellyfish was actually actuated horizontally in a tank to minimize the effect of buoyancy on the motion, see Movie S2.

FIG. 7. Pre-curved segments enable pneumatic efficiency and accuracy. (a) Using a pool of n=56 sets of randomly generated input trajectory data, we examine the effect of using pre-curved actuators on two metrics: pressure range utilization ( $p=9\times10^{-25}$ ) and pneumatic surplus (p=3×10<sup>-11</sup>). To investigate the effects on pneumatic efficiency in the case of the diaphragm, (b) the input trajectory data is taken from the curvature of the right hemisphere of the diaphragm in a coronal plane and sagittal plane MRI data, sourced from Mankodi, et al <sup>15</sup>. The sagittal plane diaphragm curvature is divided into an anterior (SA) and posterior (SP) half. (c) The pneumatic actuation parameters output from the optimization and their functional ranges are plotted for the three input trajectories. (d) The percent error is calculated for the input vs. output link lengths and bend angles for the three fields of diaphragm motion. For each trajectory, link length error (coronal motion, p=0.008; SA motion, p=0.008; SP motion, p=0.02) is calculated for 2 links at four configurations (n=8) and 1 bend angle error is calculated for each configuration (n=4), (e) Qualitatively, the higher accuracy of the optimization with precurved actuators is evident in the optimization results from input derived from the coronal plane. Boxplots show the interquartile range in blue. The median is shown in red. A Wilcoxon signed rank test is used. \*p<0.05,\*\*p<0.01,\*\*\*p<0.001

FIG. 1. Schematic of the introduction of pre-curved segments into the design optimization process.

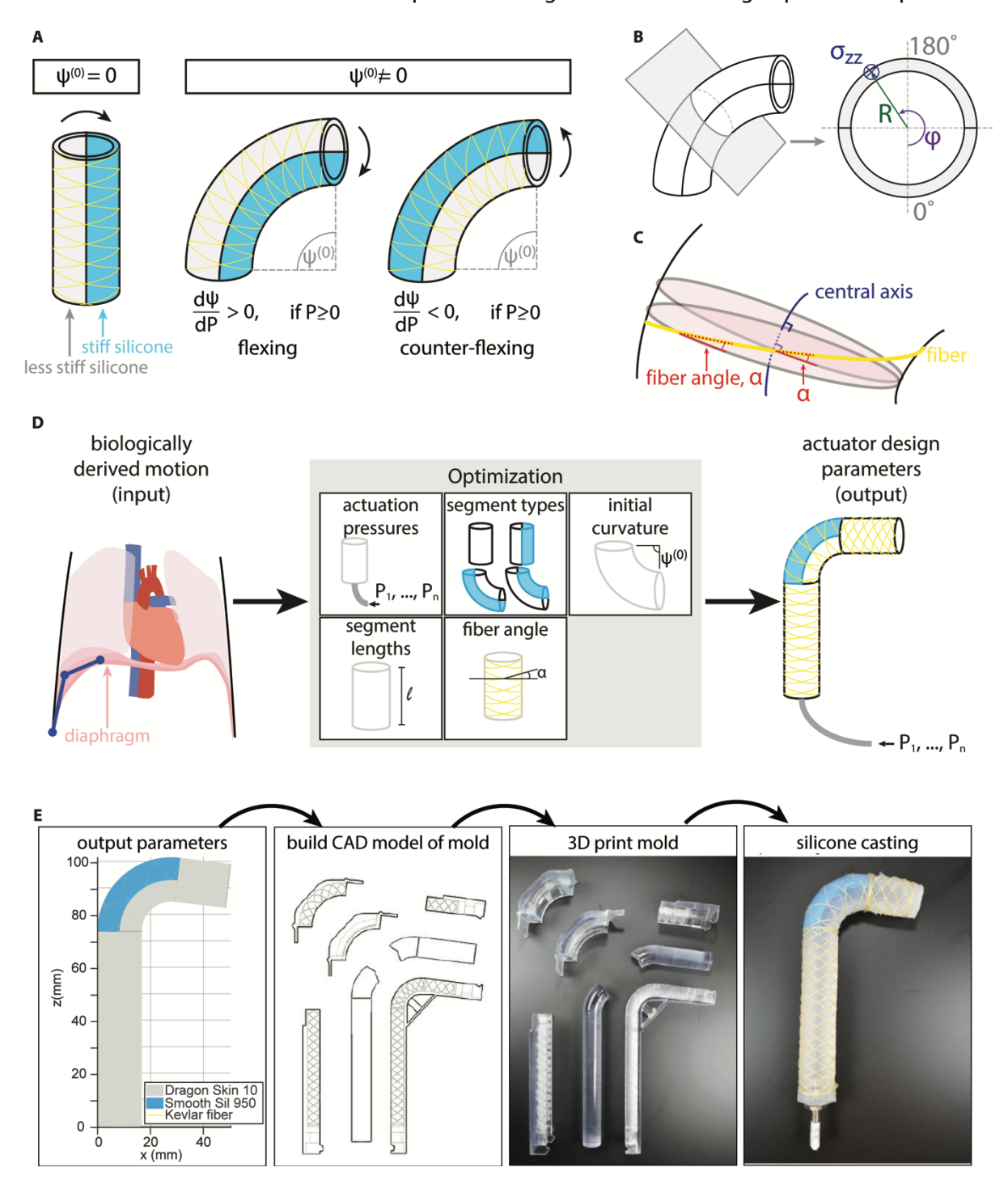


FIG. 2 Validating the analytical model via finite element analysis.

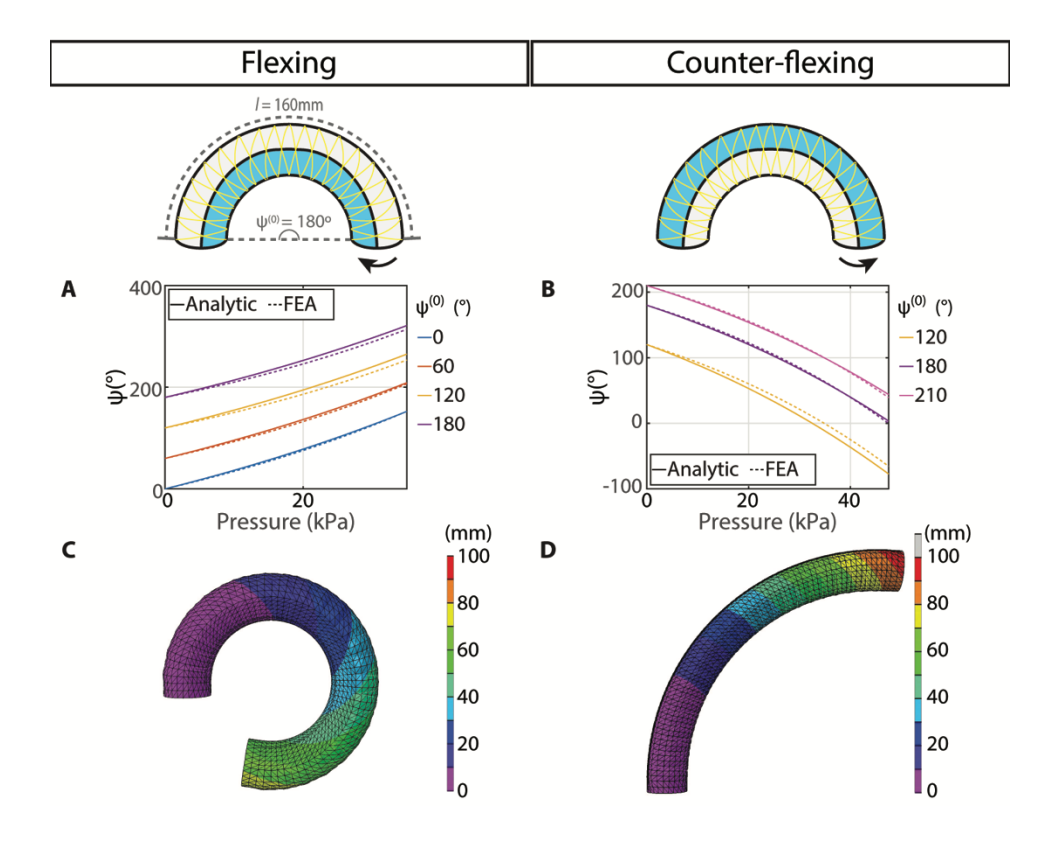


FIG. 3 Validating the analytical model with experimental results.

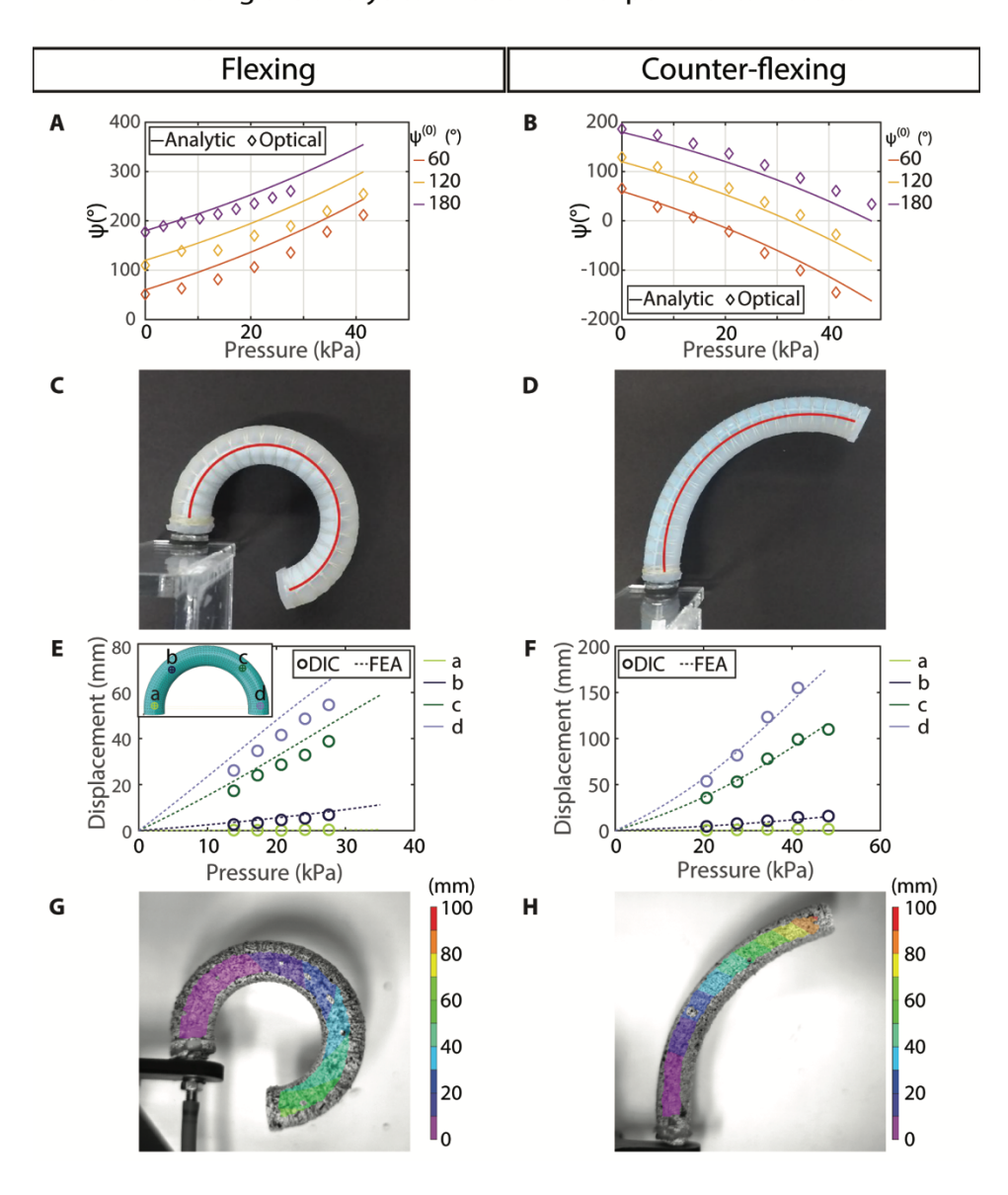


FIG. 4. Accuracy of the optimization with the inclusion of an initial bend angle,  $\psi^{(0)}$ .

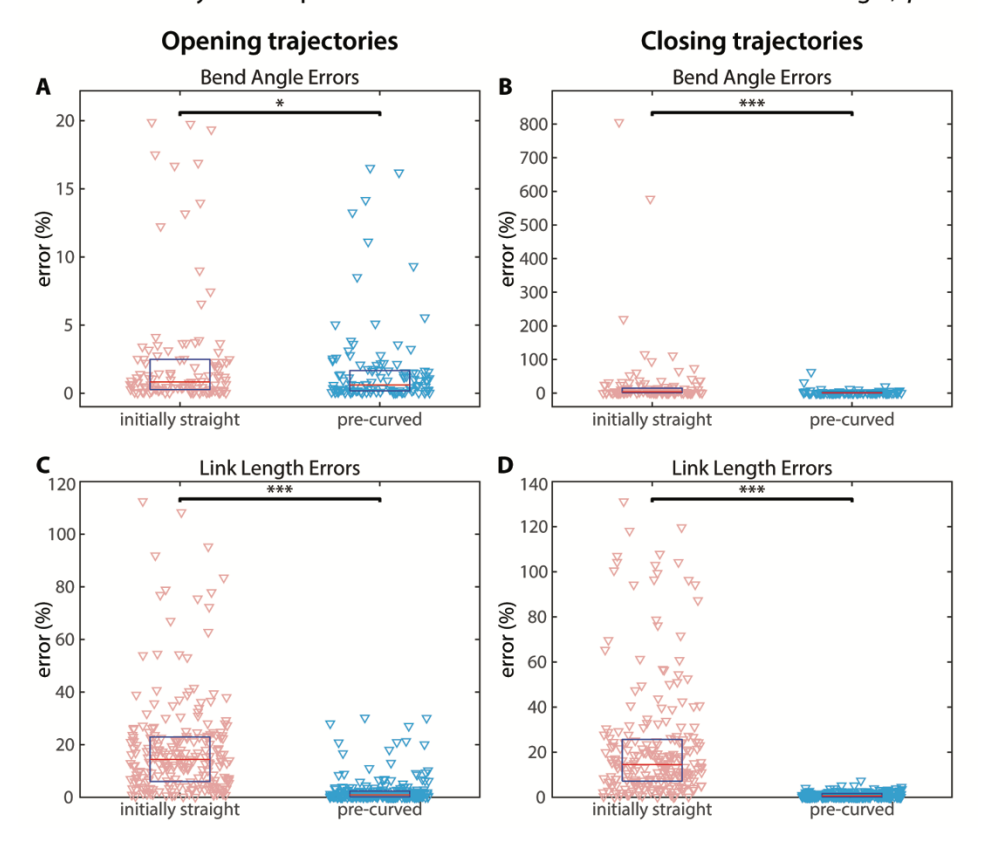


Fig. 5. Pre-curved actuators designed to follow diaphragmatic motion in exhalation.

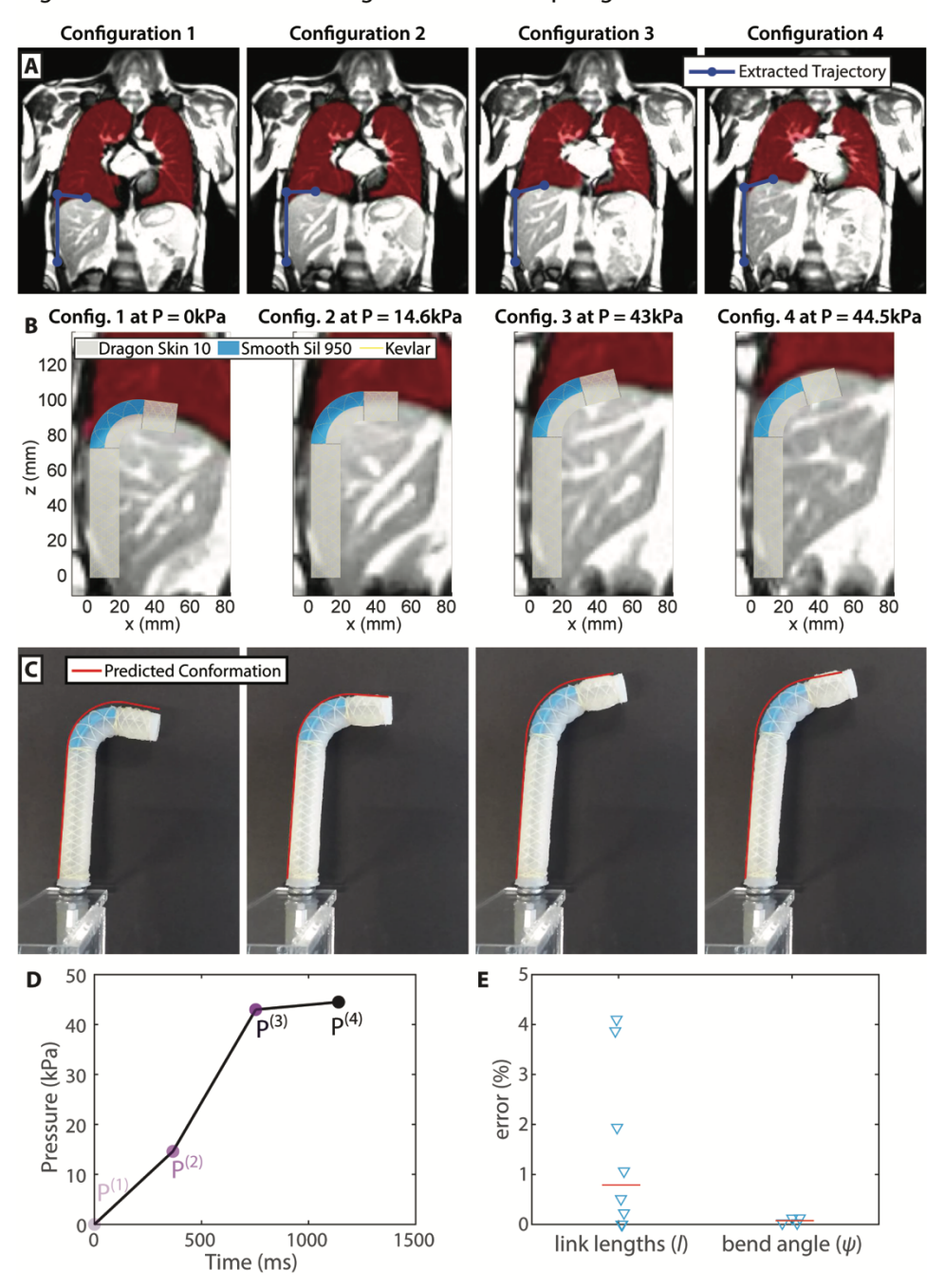


Fig. 6. Replicating planar motion with fiber reinforced actuators allows us to spatially couple actuators together to replicate 3-dimensional motion.

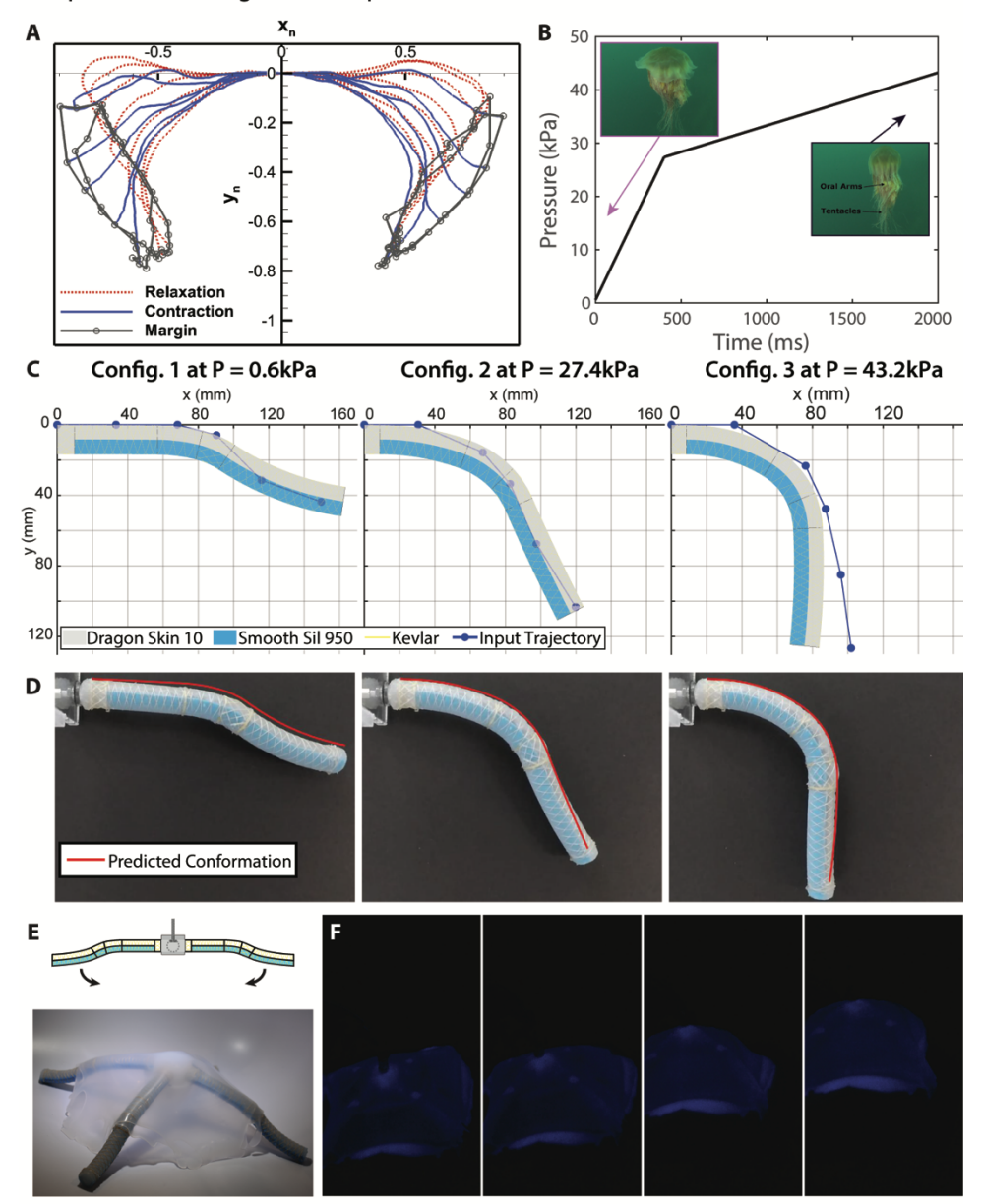
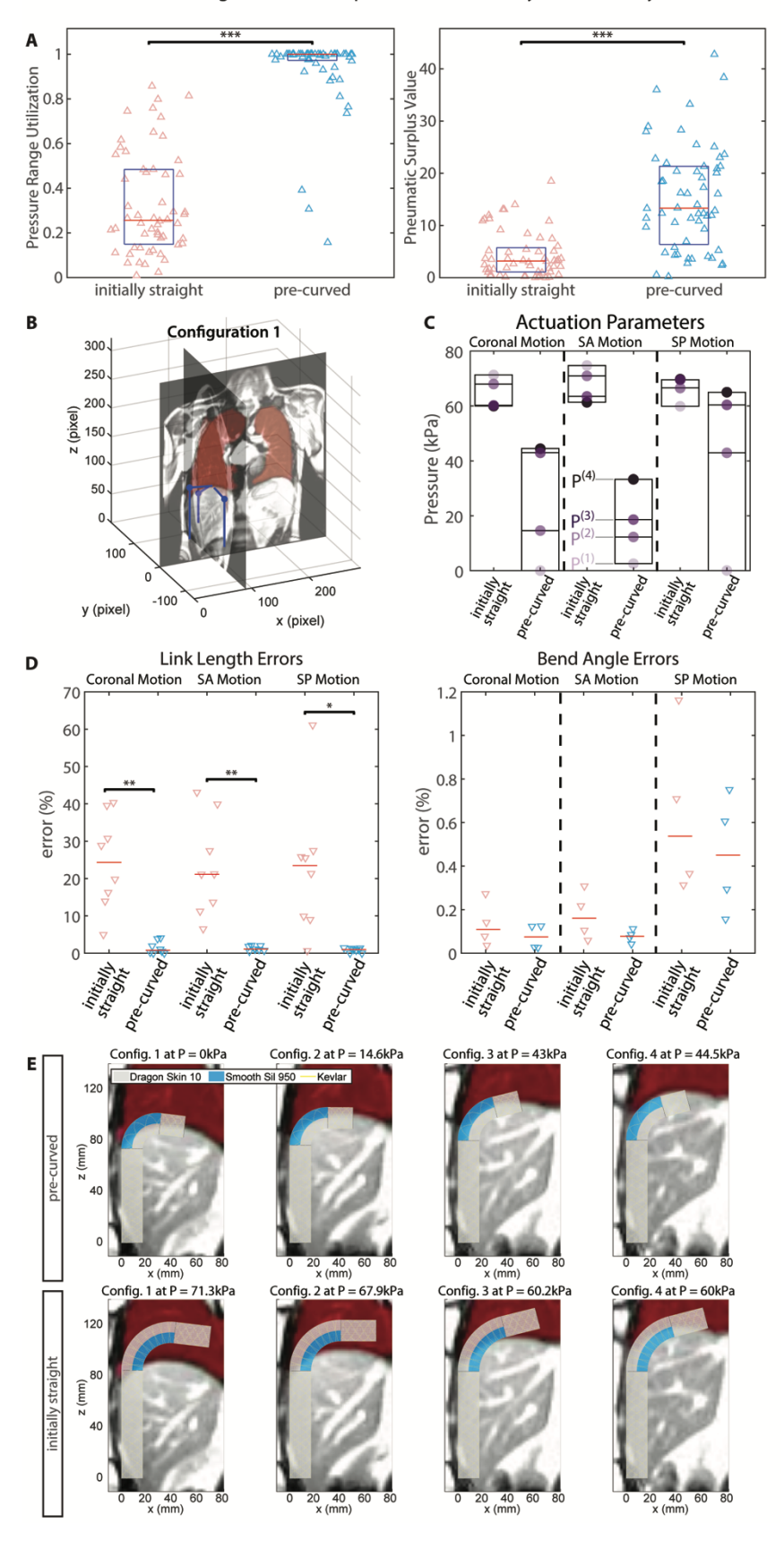


FIG. 7. Pre-curved segments enable pneumatic efficiency and accuracy.



# **Supplementary Materials**

#### Title

Pre-curved, fiber-reinforced actuators enable pneumatically efficient replication of complex biological motions.

#### Authors

Lucy Hu<sup>1,2</sup>, Dominik Gau<sup>3</sup>, James Nixon<sup>4</sup>, Melissa Klein<sup>5</sup>, Yiling Fan<sup>5</sup>, Gary Menary<sup>4</sup>, Ellen T. Roche<sup>1,2,5\*</sup>

#### **Affiliations**

<sup>1</sup>Harvard-MIT Program in Health Sciences and Technology, Massachusetts Institute of Technology, Cambridge, MA, USA.

<sup>2</sup>Institute of Medical Engineering and Sciences, Massachusetts Institute of Technology, Cambridge, MA, USA.

<sup>3</sup>Department of Mechanical Engineering, Technical University of Munich, Garching, Germany <sup>4</sup>School of Mechanical and Aerospace Engineering, Queens University, Belfast, Northern Ireland, UK.

<sup>5</sup>Department of Mechanical Engineering, Massachusetts Institute of Technology, Cambridge, MA, USA.

\*Corresponding author. Email: etr@mit.edu

# Optimization algorithm details

The great promise of soft robotic research is its capability to fulfill applications where traditional, hard-bodied robots fail. In several cases, such applications include the challenge for soft robotic actuators to perform desired motions of high complexity and therefore, affect their design parameters. In the subsequent section, an approach for the computational optimization of design parameters for a segmented actuator, which is comprised of sections of different lengths and actuator types for a given desired trajectory will be presented.

The design optimization algorithm consists of an objective function which is minimized using a trust-region method which is carried out with the MATLAB function Isqnonlin (MathWorks, Natick, MA, USA). For the objective function to be optimized, the analytical equations for extending and expanding, twisting, flexing and counter-flexing actuators have to be solved for a given input trajectory which is discretized in its link lengths  $l_{link}$ , bend angles  $\psi$  and twist angles  $\theta$  in  $n_{config}$  configurations (example given in Figures S1A and S1B). For every extending/expanding and twisting segment, the inflation-extension-torsion problem is solved for the axial stretch  $\lambda_z$  and the twist angle  $\theta$ , respectively. The objective function computes the weighted quadratic errors of the achieved solution compared to corresponding desired quantities and reads

$$f(\underline{x}) = w_{twist} \sum_{j=1}^{n_{config}} \sum_{i=1}^{n_{twist}} \left| \theta_{i}^{(j)}(\underline{x}) - \hat{\theta}_{i}^{(j)} \right|^{2} + w_{link} \sum_{j=1}^{n_{config}} \sum_{i=1}^{n_{link}} \left| l_{link,i}^{(j)}(\underline{x}) - \hat{l}_{link,i}^{(j)} \right|^{2}$$

$$+ w_{flex} \sum_{j=1}^{n_{config}} \sum_{i=1}^{n_{flex}} \left| \psi_{flex,i}^{(j)}(\underline{x}) - \hat{\psi}_{flex,i}^{(j)} \right|^{2}$$

$$+ w_{counterflex} \sum_{j=1}^{n_{config}} \sum_{i=1}^{n_{counterflex}} \left| \psi_{counterflex,i}^{(j)}(\underline{x}) - \hat{\psi}_{counterflex,i}^{(j)} \right|^{2}$$

$$(1)$$

where the superscript  $\widehat{\blacksquare}$  denotes the desired quantities describing the trajectory for every configuration  $j=1,\ldots,n_{config}$  and the expressions  $\blacksquare(\underline{x})$  are the corresponding solutions for a given set of design parameters condensed in a vector  $\underline{x}$ . The index i displays the iterator for predefined number of each segment type  $n_{type}$  and  $w_{type}$  is the respective weight. The design parameter vector  $\underline{x}$  holds explicit information about the specifications for the fabrication of a segmented actuator and the pressure values to satisfy the desired trajectory in every given configuration:

$$\underline{x} = \begin{bmatrix} P_1, \dots, P_{n_{config}} \\ \alpha_1, \dots, \alpha_{n_{twist}} & \alpha_1, \dots, \alpha_{n_{ext}} & \alpha_1, \dots, \alpha_{n_{flex}} & \alpha_1, \dots, \alpha_{n_{counterflex}} \\ l_{twist,1}^{(0)}, \dots, l_{twist,n_{twist}}^{(0)} & l_{flex,1}^{(0)}, \dots, l_{flex,n_{flex}}^{(0)} \\ l_{counterflex,1}^{(0)}, \dots, l_{counterflex,n_{counterflex}}^{(0)} \\ \psi_{flex,1}^{(0)}, \dots, \psi_{flex,n_{flex}}^{(0)} & \psi_{counterflex,1}^{(0)}, \dots, \psi_{counterflex,n_{counterflex}}^{(0)} \end{bmatrix}$$

$$(2)$$

In contrast to the optimization algorithm presented by Connolly et al. (14), the weights are not prescribed by user preference. Here, the weights are evaluated following a deviate-based weighting scheme, that is, the weights are determined according to the deviation in the input variables. In this sense, each weight is defined by the reciprocal of the variances of the corresponding input data:

$$\begin{aligned} w_{twist} &= \sigma_{twist}^{-2} \\ w_{link} &= \sigma_{link}^{-2} \\ w_{flex} &= \sigma_{flex}^{-2} \\ w_{counterflex} &= \sigma_{counterflex}^{-2} \end{aligned} \tag{3}$$

The variances can be immediately computed for required  $\hat{\theta}_i^{(j)}$ ,  $\hat{l}_{link,i}^{(j)}$ ,  $\hat{\psi}_{flex,i}^{(j)}$ ,  $\hat{\psi}_{counterflex,i}^{(j)}$  and their corresponding means  $\overline{\theta}_i^{(j)}$ ,  $\overline{l}_{link,i}^{(j)}$ ,  $\overline{\psi}_{flex,i}^{(j)}$ ,  $\overline{\psi}_{counterflex,i}^{(j)}$  as

$$\sigma_{twist}^{2} = \frac{\sum_{j=1}^{n_{config}} \sum_{i=1}^{n_{twist}} \left( \widehat{\theta}_{i}^{(j)} - \overline{\theta}_{i}^{(j)} \right)}{\left( n_{config} + n_{twist} - 1 \right)}$$

$$\sigma_{link}^{2} = \frac{\sum_{j=1}^{n_{config}} \sum_{i=1}^{n_{link}} \left( \widehat{l}_{link,i}^{(j)} - \overline{l}_{link,i}^{(j)} \right)}{\left( n_{config} + n_{link} - 1 \right)}$$

$$\sigma_{flex}^{2} = \frac{\sum_{j=1}^{n_{config}} \sum_{i=1}^{n_{flex}} \left( \widehat{\psi}_{flex,i}^{(j)} - \overline{\psi}_{flex,i}^{(j)} \right)}{\left( n_{config} + n_{flex} - 1 \right)}$$

$$\sigma_{counterflex}^{2} = \frac{\sum_{j=1}^{n_{config}} \sum_{i=1}^{n_{counterflex}} \left( \widehat{\psi}_{counterflex,i}^{(j)} - \overline{\psi}_{counterflex,i}^{(j)} \right)}{\left( n_{config} + n_{counterflex} - 1 \right)}$$

$$(4)$$

For the evaluation of the error in the link lengths  $l_{link,i}^{(j)}$ , the lengths for each link have to be computed based on which actuator segment is part of this link. The calculation of  $l_{link,i}^{(j)}$  reads in general form:

$$l_{link,i}^{(j)} = \sum_{k=1}^{n_{twist \cap link,i}} l_{twist \cap link.i_k}^{(0)} + \Delta l_{twist \cap link.i_k}^{(j)} + \sum_{k=1}^{n_{ext \cap link,i}} l_{ext \cap link.i_k}^{(0)} + \Delta l_{ext \cap link.i_k}^{(j)} + \sum_{k=1}^{n_{flex \cap link,i}} l_{flex \cap link.i_k}^{(0)} + \Delta l_{flex \cap link.i_k}^{(j)} + \Delta l_{flex \cap link.i_k}^{(j)} + \Delta l_{counterflex \cap link,i_k}^{(0)} + \sum_{k=1}^{n_{counterflex \cap link,i_k}} l_{counterflex \cap link.i_k}^{(0)} + \Delta l_{counterflex \cap link.i_k}^{(j)}$$

where the subscript  $type \cap link$ , i refers to an actuator segment being part of the corresponding link i. The length of a twisting and an extending segment is hereby computed in terms of the axial stretch given by the analytical solution for the current set of design parameters:

$$l_{twist \cap link.i_{k}}^{(0)} + \Delta l_{twist \cap link.i_{k}}^{(j)} = \lambda_{z,twist \cap link.i_{k}} l_{twist \cap link.i_{k}}^{(0)}$$

$$l_{ext \cap link.i_{k}}^{(0)} + \Delta l_{ext \cap link.i_{k}}^{(j)} = \lambda_{z,ext \cap link.i_{k}} l_{ext \cap link.i_{k}}^{(0)}$$

$$(6)$$

In the case of a flexing or counter-flexing segment, they always connect two consecutive links and so, only a fraction of their lengths contributes to the corresponding link length. Therefore,

we consider the relation between the bend angle  $\psi$ , the radius of curvature  $\rho$  and the demanded length x:

$$\tan\left(\frac{\psi}{2}\right) = \frac{x}{\rho} \tag{7}$$

Making use of the approximation for small angles  $\tan\left(\frac{\psi}{2}\right) \approx \frac{\psi}{2}$ , Eq. (7) can now be rewritten, yielding half of the actuator segment length:

$$x = \frac{\psi}{2}\rho = \frac{1}{2}l\tag{8}$$

Further, the elongation of the outermost material line of a pre-curved tube upon a given deflection with respect to the geometrical quantities describing the actuator cross-section is:

$$\Delta l = (\psi - \psi^{(0)}) R_o (1 + \cos(\overline{\varphi})) \tag{9}$$

Finally, the length contribution of flexing and counter-flexing segments to link i using Eqs. (8) and (9) can be derived:

$$\frac{1}{2} \left( l_{flex \cap link.i_k}^{(0)} + \Delta l_{flex \cap link.i_k}^{(j)} \right) \\
= \frac{1}{2} \left( l_{flex \cap link.i_k}^{(0)} \left( \psi_{flex \cap link.i_k}^{(j)} - \psi_{flex \cap link.i_k}^{(0)} \right) R_o (1 + \cos(\overline{\varphi})) \right) \tag{10}$$

$$\frac{1}{2} \left( l_{counterflex \cap link.i_{k}}^{(0)} + \Delta l_{counterflex \cap link.i_{k}}^{(j)} \right) \\
= \frac{1}{2} \left( l_{counterflex \cap link.i_{k}}^{(0)} \left( \psi_{counterflex \cap link.i_{k}}^{(j)} - \psi_{counterflex \cap link.i_{k}}^{(0)} \right) R_{o}(1 + \cos(\overline{\varphi})) \right)$$
(11)

The computed errors for the current set of design parameters are then compared to a predefined tolerance. If the function value is still above the threshold, a new set of design parameters will be determined according to a trust-region method and the whole procedure is repeated until the function holds a value beneath the tolerance. The detailed formulation denotes a constrained optimization problem in the form

minimize 
$$f(\underline{x}), \quad \underline{x} \in \mathbb{R}^n$$
  
subject to  $\underline{h}(\underline{x}) \le \underline{0} \quad \underline{h} \in \mathbb{R}^q$  (12)

where  $\underline{h}$  is a vectorial function describing an inequality constraint which arises from boundaries that are determined to restrict the permitted range for each design parameter, so that actuator fabrication is still possible, The inequality constraint with lower and upper bounds  $\underline{x}_{min}$  and  $\underline{x}_{max}$  therefore reads as follows:

$$\underline{h}(\underline{x}) = \begin{bmatrix} \underline{x} - \underline{x}_{max} \\ x_{min} - x \end{bmatrix} \le \underline{0} \tag{13}$$

# Finding the neutral axis

The analytical model assumes, for the sake of simplicity, the axial stretch in the case of planar bending based on the Euler-Bernoulli beam theory [3] and therefore describes a bending deformation within the cross-section with respect to a neutral axis, that is the location where no deformation appears throughout the tube and subsequently is stress-free. The location of the neutral axis is defined by the circumferential coordinate  $\overline{\varphi}$ . In order to determine the parameter value via FEM, material lines on the outer surface along the central actuator axis located at a distinct circumferential position analogous to the neutral axis have been defined. We further assume the neutral axis to appear within the region of the strain-limiting Smooth Sil 950 layer and therefore the circumferential coordinate for material lines in the case of bending are defined by  $\overline{\varphi} = \{0, 25, 35, 45, 90, 180\}^{\circ}$  and  $\overline{\varphi} = \{0, 90, 130, 150, 160, 180\}^{\circ}$  in terms of a straightening actuator. For each actuator type, one simulation was conducted according to with symmetrical fibers with fiber angles  $\alpha = 5^{\circ}$  and  $\beta = -5^{\circ}$ , respectively. For both simulations, the application of a linearly increasing pressure onto the actuator inner, fluidic cavity leads to a continuously and monotonously altering bend angle for each deformed configuration. In order to identify the location of the neutral axis for bending and straightening, the global coordinates of element nodes for each material line is exported. Subsequently, the coordinates are sorted and the length of each material line is computed by the sum of distances between all neighboring nodes. Comparing the lengths for deformed configurations at t > 0 with the length in the undeformed configuration at t = 0 gives the axial stretch for every material line in each time step. The neutral axis is characterized is the material line at which the stretch remains 1 for every deformed configuration. Following this, the neutral axis for bending could be identified at  $\bar{\varphi} = 35^{\circ}$  and in terms of straightening at  $\bar{\varphi} = 150^{\circ}$  from the corresponding FEM results, seen in Fig. S2.

# **Analytical solution derivation**

Connolly et al. (16) and Polygerinos et al. (12) showed that the kinematics of flexing actuators can be derived by evaluating the equilibrium of moments around the neutral bending axis on the capped, unfixed end. The balance of moments is expressed as the comparison of the resulting force of the internal pressure acting on the cap and the material response of the semicylindrical layers as displayed in Figure S3A. Within an infinitesimal small region close to the capped end we can assume that the radial expansion can be neglected, so that r = R and consequently the radial stress component vanishes  $\sigma_{rr} = 0$  and additionally, since the actuators are designed to

always yield two families of symmetrical fibers with fiber angles  $\alpha = -\beta$ , no twisting around the actuator axis takes place  $\tau = 0$ . The deformation gradient and the left Cauchy-Green deformation tensor hence read

$$\underline{F} = \begin{bmatrix} \lambda_z^{-1} & 0 & 0 \\ 0 & 1 & 0 \\ 0 & 0 & \lambda_z \end{bmatrix} \tag{14}$$

$$\underline{b} = \begin{bmatrix} \lambda_z^{-2} & 0 & 0 \\ 0 & 1 & 0 \\ 0 & 0 & \lambda_z^2 \end{bmatrix} \tag{15}$$

which just display dependence in the axial stretch due to flexing or counter-flexing  $\lambda_z$ . In this model, the curvature in the bent configuration is constant across the whole actuator and the cross-sections are assumed to remain perpendicular along the actuator axis. In contrast to initially straight flexing actuators, material lines parallel to the actuator axis along the whole body are not uniform across the cross-section. In this way, a flexing or counter-flexing actuator is, in addition to the initial bend angle  $\psi^{(0)}$ , characterized by its length measured on the outermost material line which corresponds to a circumferential angle  $\varphi=180^\circ$  within the cross-section. We can use this information to formulate a generalized axial stretch of a cylinder due to flexing or counter-flexing in dependence of an arbitrary point within the cross-section:

$$\lambda_z = \frac{l - \psi^{(0)} R_o (1 + \cos(\bar{\varphi})) + \psi(R_o \cos(\bar{\varphi}) - R \cos(\varphi))}{l - \psi^{(0)} (R_o + R \cos(\varphi))}$$
(16)

In Eq. (1)  $\psi$  denotes the bend angle in the current configuration,  $\varphi$  and R depict the circumferential coordinate  $0^{\circ} \leq \varphi \leq 180^{\circ}$  and the radius  $R_i \leq R \leq R_o$  characterizing the point in the cylindrical cross-section, at which the axial stretch is computed and  $\bar{\varphi}$  is the location of the neutral axis for flexing or counter-flexing. The actuator is comprised of two different elastomeric materials which mechanical response is approximated by the isotropic, incompressible Neo-Hookean strain energy and reinforced by two families of symmetrical fibers with the corresponding terms:

$$\Psi_{elastomer} = \frac{\mu}{2}(I_1 - 3) \tag{17}$$

$$\Psi_{fiber} = \frac{E_{fiber}}{2} \left(\sqrt{I_4} - 1\right)^2 + \frac{E_{fiber}}{2} \left(\sqrt{I_6} - 1\right)^2 \tag{18}$$

In Eq. (17),  $\mu$  depicts the shear modulus of the elastomer and  $I_1$  the sum of the corresponding quadratic principal stretches. The strain energy density of the fibers is assumed to yield a linear elastic stress-strain relationship where  $E_{fiber}$  denotes the fibers' elastic modulus and  $I_4$  and  $I_6$  are the quadratic stretches in fiber direction for each family. It should be noted that the fibers are not

dispersed within the elastomeric matrix but are wrapped around the outer surface of the tube. Therefore, the actuator is further described by a layered design as illustrated in Figure S3B, subdividing the cross-section into an inner, isotropic layer of homogenous elastomer for  $R_i \leq R \leq R_m$  and a thin outer, anisotropic layer composed of elastomer and fibers for  $R_i \leq R \leq R_o$ . In this sense, each of the layers can be associated with a strain energy composed of its constituent strain energy functions and weighted by the corresponding volume fractions  $\rho$ , respectively:

$$\Psi_i = \Psi_{elastomer} \tag{19}$$

$$\Psi_o = \rho_{elastomer} \Psi_{elastomer} + \rho_{fiber} \Psi_{fiber}$$
 (20)

The material response upon deformation of each layer can now be computed by the Cauchy stress tensor for the incompressible case in terms of the corresponding strain energy function, its invariants and a not specified hydrostatic pressure p and reads

$$\underline{\underline{\sigma}_{i}} = 2 \frac{\partial \Psi_{elastomer}}{\partial I_{1}} \underline{\underline{b}} - p\underline{\underline{I}}$$
(21)

$$\underline{\underline{\sigma}}_{o} = \rho_{elastomer} \left( 2 \frac{\partial \Psi_{elastomer}}{\partial I_{1}} \underline{\underline{b}} \right) + \rho_{fiber,1} \left( 2 \frac{\partial \Psi_{fiber}}{\partial I_{4}} \underline{\underline{s}}_{1} \otimes \underline{\underline{s}}_{1} \right) + \rho_{fiber,2} \left( 2 \frac{\partial \Psi_{fiber}}{\partial I_{6}} \underline{\underline{s}}_{2} \otimes \underline{\underline{s}}_{2} \right) - p\underline{\underline{I}}_{\underline{b}}$$

$$(22)$$

where  $\underline{s}_n = \underline{F} \underline{S}_n$ , n = 1,2 is the deformed fiber direction expressed as the push-forward of the reference fiber alignment  $\underline{S}_1 = [0, \cos(\alpha), \sin(\alpha)]^T$  and  $\underline{S}_2 = [0, \cos(\beta), \sin(\beta)]^T$ . The axial stress due to bending in a material point within the cylindrical, pure elastomeric cross-section can be derived via elimination of the hydrostatic pressure term in Eq. (21) under the assumption of vanishing radial stresses  $\sigma_{rr} = 0$ :

$$\sigma_{i,zz} = \mu(\lambda_z^2 - \lambda_z^{-2}) \tag{23}$$

Note that this expression is just valid for the inner, isotropic layer. For the outer layer the contribution of the anisotropic part as in Eq. (22) has to be added and every term has to be weighted with the corresponding volume fraction:

$$\sigma_{o,zz} = \rho_{elastomer} \left( \mu(\lambda_z^2 - \lambda_z^{-2}) \right) + \rho_{fiber,1} \left( 2E_{fiber} \frac{\sqrt{I_4} - 1}{\sqrt{I_4}} \lambda_z^2 \sin(\alpha)^2 \right)$$

$$+ \rho_{fiber,2} \left( 2E_{fiber} \frac{\sqrt{I_6} - 1}{\sqrt{I_6}} \lambda_z^2 \sin(\beta)^2 \right)$$
(24)

The material response of the tube due to axial deformation upon bending, that is the deformed bend angle, is governed by a passive moment around the neutral axis acting against the inflation, the moment with respect to the deformed quantities reads as follows:

$$M_{mat}(\psi) = 2 \int_{0}^{\pi} \int_{r_{i}}^{r_{o}} \sigma_{zz}(r_{o}\cos(\bar{\varphi}) - r\cos(\varphi)) r dr d\varphi$$
(25)

Substitution of r to R, usage of the relation  $\frac{dr}{dR} = \lambda_z^{-1}$  and geometrical subdivision according to the predefined layered actuator design, the final form for the moment originating from the material depicts:

$$M_{mat}(\psi) = 2 \int_{0}^{\pi} \int_{R_{i}}^{R_{o}} \sigma_{zz}(R_{o} \cos(\bar{\varphi}) - R \cos(\varphi)) R \frac{dr}{dR} dR d\varphi$$

$$= 2 \int_{0}^{\pi} \int_{R_{i}}^{R_{o}} \sigma_{zz} \lambda_{z}^{-1} R(R_{o} \cos(\bar{\varphi}) - R \cos(\varphi)) dR d\varphi$$

$$= 2 \int_{0}^{\pi} \int_{R_{i}}^{R_{m}} \sigma_{i,zz} \lambda_{z}^{-1} R(R_{o} \cos(\bar{\varphi}) - R \cos(\varphi)) dR d\varphi$$

$$+ 2 \int_{0}^{\pi} \int_{R_{m}}^{R_{o}} \sigma_{o,zz} \lambda_{z}^{-1} R(R_{o} \cos(\bar{\varphi}) - R \cos(\varphi)) dR d\varphi$$

$$(26)$$

On the other hand, the active moment around the neutral axis as a consequence of the applied pressure can be derived by integrating the force on an infinitesimal horizontal line element on the cap  $df = 2Pr_i^2 \sin(\varphi)^2 d\varphi$  across its surface and substituting from r to R, so that

$$M_{cap}(P) = \int_{0}^{\pi} (r_o \cos(\bar{\varphi}) - r_i \cos(\varphi)) df$$
$$= 2PR_i^2 \int_{0}^{\pi} \sin(\varphi)^2 (R_o \cos(\bar{\varphi}) - R_i \cos(\varphi)) df$$
 (27)

which depicts a function with respect to the internal pressure *P*. Now we can define the objective function for modeling flexing and counter-flexing motion by evaluating the equilibrium of moments around the neutral axis:

$$f_{EoM}(\psi, P) = M_{mat}(\psi) - M_{cap}(P) = 0$$
 (28)

This function holds dependence in the current bend angle  $\psi$  and the applied pressure P and can be evaluated in two ways, either solving for the current actuator pose  $\psi$  at a given pressure P or vice versa.

#### Calibration for the analytical model based on FEA data

The calibration process gives optimized model parameters with respect to minimizing the squared error between the analytical and the FEM solution which were identified as the effective shear modulus  $\bar{\mu}=0.084302MPa$  and the anisotropic layer thickness t=0.0022742mm in the case of flexing and corresponding to a counter-flexing actuator these quantities read  $\bar{\mu}=0.081179MPa$  and t=0.00051264mm. These values approximate those found by Connolly et al. (14) of  $\bar{\mu}=0.78MPa$  and t=0.000889mm for their initially straight bending actuator. Fig. S4A,B displays the result in qualitative manner, visualizing corresponding pressure-bend angle curves for each fiber angle. For counter-flexing motions, the calibrated model depicts qualitatively well-fitting results as can be seen from belonging curves in Fig. S4B.

Due to the long fabrication time of these actuators, we opt to test a subset of cases of fiber angle  $\alpha = [5^\circ, 15^\circ]$ . We cross-validate the analytical model via our experimental tracking, seen in Fig. S4C,D. We notice that in the counter-flexing experiment, there is some overlap between the experimental data. This is largely attributed to the deviation from the initial fabricated bend angle (note that the  $\alpha = 5^\circ$  in Fig. S4D has a consistently inflated bend angle offset from the predicted curve). This indicates that if the actuator were fabricated to begin with an initial bend angle of 180°, we would see the curves separate and better match our analytical model. This does indicate the importance of a consistent manufacturing method. Overall, we find that the optical tracking matches the overall trends and behavior predicted by the analytical model. Future validation should expand the fiber angles tested to higher values.

# **Supplementary Materials and Methods Silicone molding of pre-curved actuators**

Utilizing pre-curved actuators trades ease of manufacturing for more accurate and efficient actuators. To create these actuators, we 3D-print our multi-part mold using an Objet30 Prime printer. The mold for the pre-curved actuators with an initial bend angle of 180° tested in Fig. 2 is shown in Fig. S5A. Component (a) molds the inner silicone layer (for which  $\varphi$  spans 0° to 90° and 270° to 360°) with the fiber grooves, component (b) is a 2-part inner core, component (c) is an aligning piece that will align the inner cores properly and also has grooves to case a "sacrificial lip" onto the first cast layer of silicone, and component (d) molds the outer silicone layer (for which  $\varphi$  spans the range of 90° to 270°) with the fiber grooves. These actuators are fabricated in a two-part fabrication process, in which the silicone molded by component (a) is cast and cured first, and then the silicone molded by component (d) is cast onto the silicone cast by component (a). For a flexing actuator, the stiffer silicone (Smooth-Sil 950) is cast by component (a), and for a counter-flexing actuator, the less stiff silicone (Dragon Skin 10 Medium) is cast by component (a).

The casting process for the first half is shown in Fig. S5B. In order to keep the silicone contained in the mold during the degassing, we clamp the "bottom" component (this is component (c) for the first silicone half and component (d) for the second silicone half) between two layers of acrylic. The mixed silicone is poured into the mold (Fig. S5B(i)). The silicone is degassed in a vacuum chamber for approximately 70% of the manufacturer's stated pot life (Fig. S5B(ii)). The inner cores are then introduced (Fig. S5B(iii)). They are pressed down into the aligning component for the first silicone layer. They are then put back in the vacuum chamber for another 20% of the stated pot life (Fig. S5B(iv)) to degas air that may have been introduced by the inclusion of the inner cores. Then the "top" component is introduced (Fig. S5B(v)). The two halves of the mold are pressed together. One acrylic layer is removed, and the two halves of the mold are clamped together (Fig. S5B(iv)). This is left to cure at room temperature according to the manufacturer's cure time. After the first layer is cured, the silicone for the second half is mixed and poured into component (d) as described earlier. As this silicone is degassing for 90% of the manufacturer's stated pot life, a scalpel is used to cut off the "sacrificial lip" revealing a fresh layer of silicone along the material lines of  $\varphi=90^{\circ}$  and  $\varphi=270^{\circ}$ . This will allow for better adhesion between this new layer of silicone and the first layer of silicone. The complex of components (a), (b), and the first layer of silicone is introduced to the degassed silicone mixture, and the mold is clamped together. This is left to cure at room temperature according to the manufacturer's cure time.

An analogous process is undergone for the multi-segment actuators output from the optimization. The multi-component molds follow the lines at which the two-materials meet on the actuator (see Fig. 1E). Fig. S5C shows the casting process for a multi-segment diaphragm actuator. The concave mold half is used as the "bottom" mold to initially cast the Dragon Skin 10 Medium layer (Fig. S5C(i)). The "aligning" mold piece occupies the space at which the Smooth-Sil 950 will occupy during the second casting step (Fig. S5C(ii)).

**Instrumentation for actuation validation experiements** 

In order to deliver automated temporal and pneumatic control, the actuators were pneumatically activated by a customized control box using SMC ITV1000 series electropneumatic regulators (SMC Corporation, Chiyoda, Tokyo, Japan) based on the valve sequencing working principle. Their deformation was captured on video via a GoPro Hero 5 (GoPro, Inc., San Mateo, CA, USA) in a 1080p linear mode of capture. The video is analyzed via a MATLAB script (MathWorks, Natick, MA, USA) which allows a user to select the appropriate representative frame of the video and relies on a basic image segmentation to isolate the actuator body from the black background. The script calculates the best fit arc to the binarized shape of the actuator body and calculates the enclosed bend angle to the extracted arc length.

Using digitial image correlation allows us to generate the full field strain maps of the actuators undergoing deformation. The paint used for the speckle patterning was aerosol Rustoleum Universal. Each individual actuator was then placed in view of two Photron FASTCAM SA.4 high speed cameras. These cameras were synchronized and running at 2000 frames per second and at full resolution 1024x1024 pixels, with each camera equipped with a Nikon Nikkor 50mm f1.8 lens. The different pressure magnitudes were then introduced into the actuators using a Festo MS6-LRP regulator (output 0-2.5bar) and a pneumatic ball valve shut-off. One second of actuator deformation was recorded and the images were imported into the correlation software Correlated Solutions VIC-3 v7. The appropriate calibration routine was performed and the correlation process (Table S1) was carried out for the entire surface of each actuator. The strain and displacement output from discrete data points were then extracted to positionally match the output from the equivalent FE simulation.

#### Setup to test biomimetic actuators

The diaphragm actuators seen in Fig. 4 and Movie S1 were fabricated via multi-component molds. In order to setup their actuation for Movie S1. An acrylic platform was laser cut to hold the actuators at the correct spacing.

The jellyfish actuators, seen in Fig. 5 and Movie S2, were coupled to a central silicone connector—made of DragonSkin 10 Medium—that was installed with a vented screw. A glow-in-the-dark silicone bell was coupled to the four-actuator setup. To fabricate this bell, a 12in x 12in PETG sheets were thermoformed over a dome to give the bell an initial dome shape in order to minimize external forces exerted by the bell on the actuators. The bell was cast by pouring two layers of DragonSkin 10 M and allowing the still liquid silicone to distribute itself across the mold. The second layer contained blue glow-in-the-dark powder—Strontium Aluminate, Europium & Dysprosium formula (TechnoGlow, Dist, Ennis, TX, USA)—mixed in a 1:5 weight ratio. The bell is attached to the actuator via 4 discrete points with a small patch of Sil-Poxy.

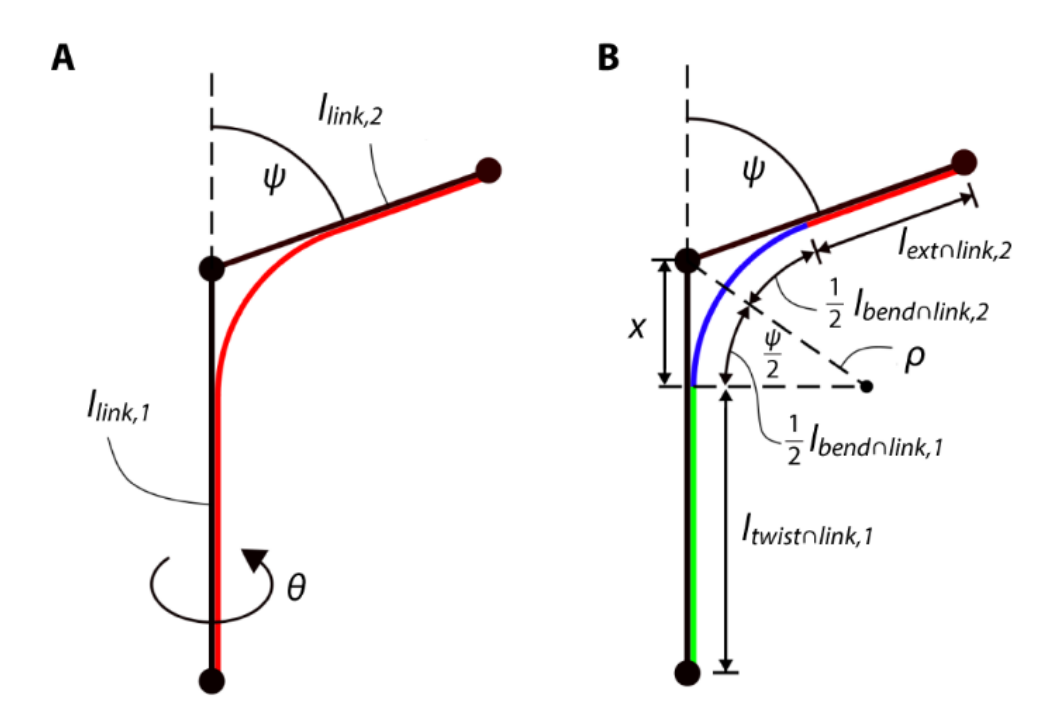


Fig. S1. Schematic of the discretization of a curvature into link lengths and bend angles. (A) Discretization of an arbitrary trajectory (red line) into a finite number of links connected by joints. (B) Diagram of definition of link lengths and bend angles from the discretized trajectory. l is the length,  $\psi$  is the bend angle, and  $\theta$  is the degree of twist.

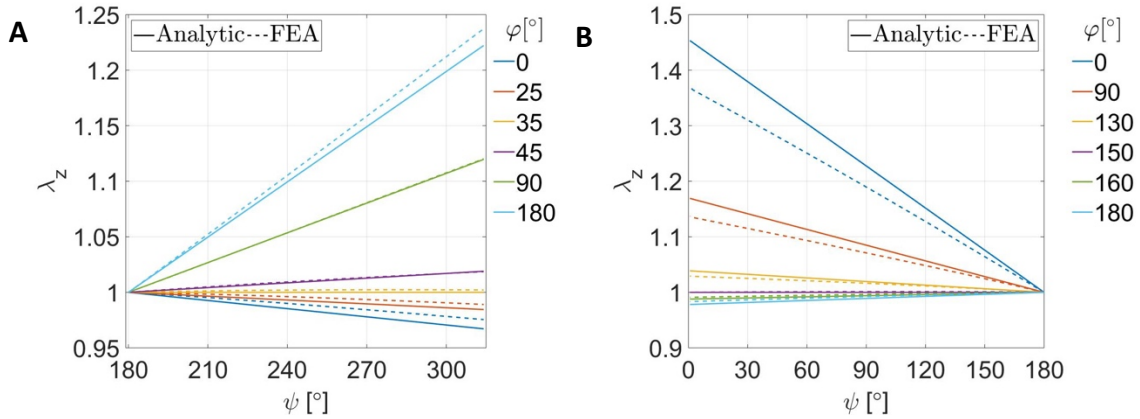


Fig. S2. Determining the location of the neutral axis. The axial stretch for the analytical and FEA model with respect to an (A) flexing and (B) counter-flexing actuator plotted for material lines along different circumferential angles,  $\varphi$ .

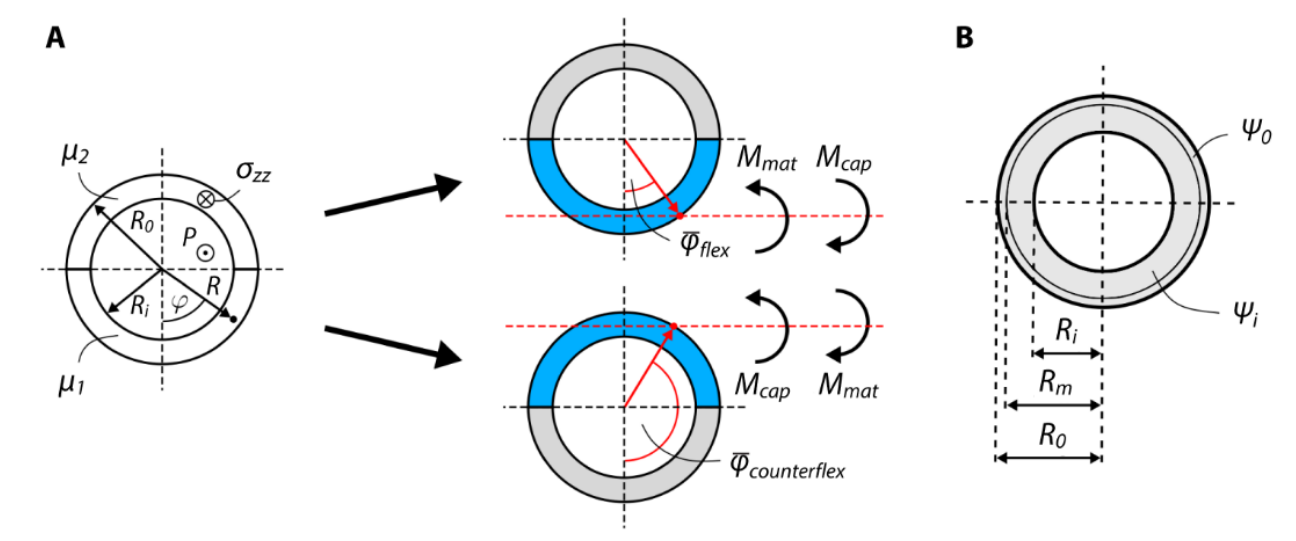


Fig. S3. Schematic of considerations for the derivation of the analytical model. A)

Illustration of bending and straightening kinematics due to inflation. The equilibrium of moments is evaluated around the neutral axis (red line) within a cross-section close to the capped, unfixed end of the tube. The applied pressure P acting on the inner surface (pointing out of plane) and the resulting axial stress  $\sigma_{zz}$  in the material (pointing inwards) generate moments resulting in a bending (top right) or straightening (bottom right) motion depending on the material alignment (strain-limiting layer is blue and inflatable layer is gray). (**B**) Cross-sectional view of the layered actuator design. The actuator is comprised of an inner, isotropic layer of homogenous material  $\Psi_i$  and an outer, anisotropic layer  $\Psi_0$ .  $R_i$  is the inner radius,  $R_0$  is the outer radius, and  $R_m$  is the radius to the assumed boundary between the isotropic and anisotropic layers.  $\bar{\varphi}$  is the circumferential angle at which the neutral axis exists.

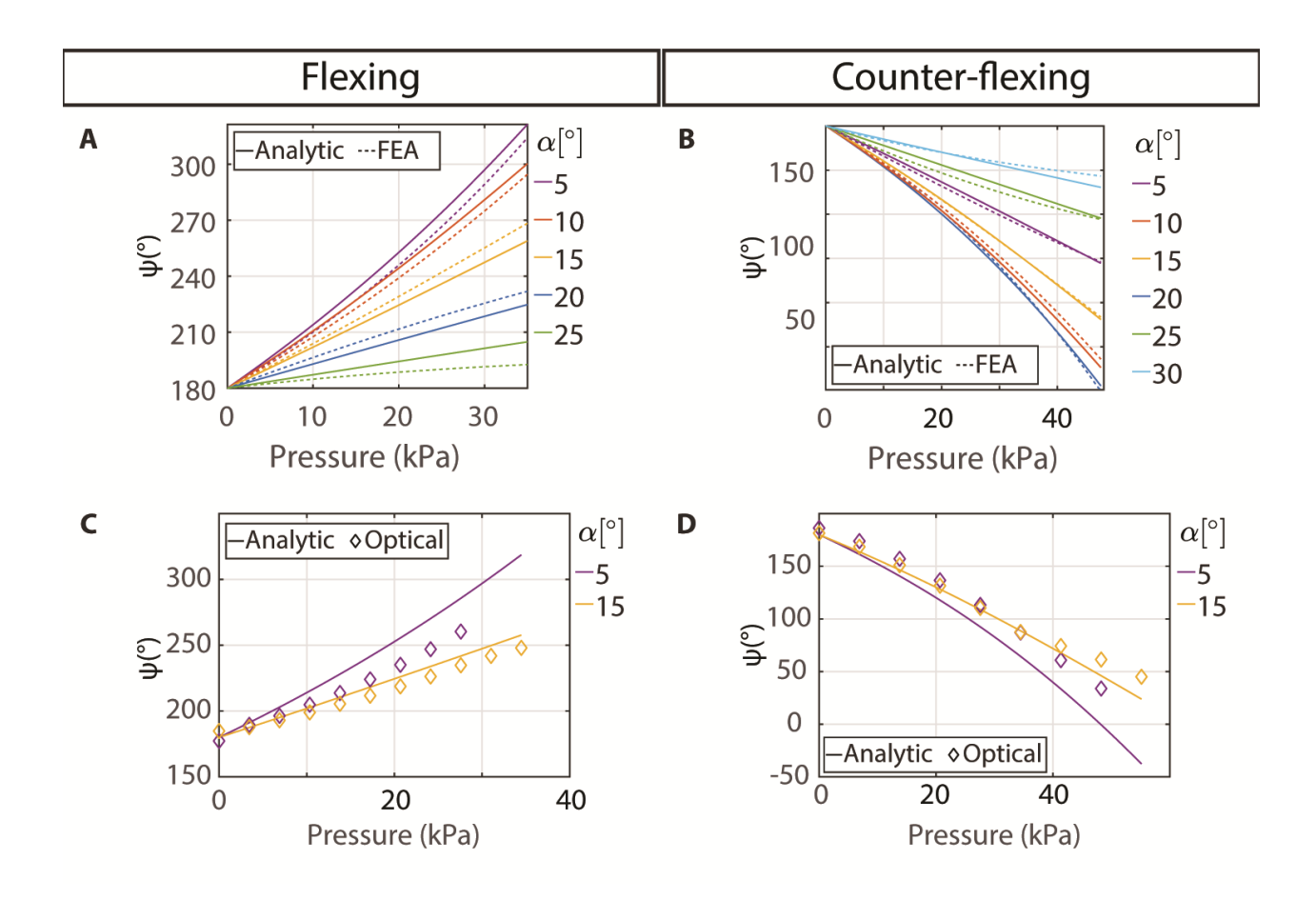


Fig. S4. Validation of analytical model for varying fiber angle,  $\alpha$ . The predicted bend angle pressure response for the analytical model and finite-element model for varying  $\alpha$  is compared for the (A) flexion and (B) counter-flexion actuators with a set initial bend angle of  $\psi^{(0)} = 180^{\circ}$  and outer length of 160 mm. The experimental bend angle pressure response determined via optical tracking is compared to the analytical model for varying  $\alpha$  for the (C) flexion and (D) counter-flexion case.



**Fig. S5 Silicone casting methods.** (**A**) 3D-printed multi-component mold for fabricating actuators with an initial bend angle of 180°. The mold is made up of: (a) a mold with inlaid grooves for fibers for the inner half of the actuator, (b) inner cores, (c) component to align the inner cores, and (d) a mold with inlaid grooves for fibers for the outer half of the actuator. (**B**) The silicone casting process depicting: (i) pouring, (ii) 1<sup>st</sup> degassing step, (iii) introduction of the inner cores, (iv) 2<sup>nd</sup> degassing step, (v) bringing the mold halves together, and (vi) clamping the mold for curing. (**C**) Analogous casting process for the multi-segment actuators to replicate diaphragm motion. (i) The concave piece is used to degas the silicone. (ii) The molds for casting the first layer require more points of clamping.

Camera set-up	Specifications
Camera type	Photron FASTCAM SA.4
Sensor type	12 bit 20μm pixel
Lens type	Nikon Nikkor 50mm f1.2
Field of view	200mmx200mm (approx.)
Calibration Results	
Panel size	14x9 (7mm)
Stereoscopic angle	20°
Focal length	580mm (approx.)
Correlation process	
Speckle size	
Step size	5
Subset size	25
Displacement resolution	1.9 µm, 0.01 pixel
Correlation method	Incremental
Smoothing method	Gaussian filter, 15

**Table S1. Table of equipment for digital image correlation (DIC).** Specifications of the experimental setup for the DIC work.

# Movie S1. Matching the motion of the diaphragm via the coronal cross-section data. Discretized trajectory data is extracted from the dynamic movement of the diaphragm via cine MRI of a healthy subject during maximal breathing from Mankodi et al (19). The fiber-reinforced actuators described in Fig. 4 are actuated and superimposed upon the binarized highlighted lung area.

**Movie S2. Visualization of luminescent jellyfish in water.** The actuators described in Fig. 5 are combined together and fitted with a UV-responsive, glow-in-the-dark powder. The combined biomimetic jellyfish is actuated in a tank of water.